https://lib.uliege.be https://matheo.uliege.be

Master thesis and internship[BR]- Master's thesis : Experimental and numerical investigations of the VIV-galloping instability of a bluff body[BR]- Integration internship

Auteur : Ambrosio, Andrea
Promoteur(s) : Andrianne, Thomas
Faculté : Faculté des Sciences appliquées
Diplôme : Master en ingénieur civil en aérospatiale, à finalité spécialisée en "aerospace engineering"
Année académique : 2024-2025
URI/URL : http://hdl.handle.net/2268.2/23381

Avertissement à l'attention des usagers :

Tous les documents placés en accès ouvert sur le site le site MatheO sont protégés par le droit d'auteur. Conformément aux principes énoncés par la "Budapest Open Access Initiative"(BOAI, 2002), l'utilisateur du site peut lire, télécharger, copier, transmettre, imprimer, chercher ou faire un lien vers le texte intégral de ces documents, les disséquer pour les indexer, s'en servir de données pour un logiciel, ou s'en servir à toute autre fin légale (ou prévue par la réglementation relative au droit d'auteur). Toute utilisation du document à des fins commerciales est strictement interdite.

Par ailleurs, l'utilisateur s'engage à respecter les droits moraux de l'auteur, principalement le droit à l'intégrité de l'oeuvre et le droit de paternité et ce dans toute utilisation que l'utilisateur entreprend. Ainsi, à titre d'exemple, lorsqu'il reproduira un document par extrait ou dans son intégralité, l'utilisateur citera de manière complète les sources telles que mentionnées ci-dessus. Toute utilisation non explicitement autorisée ci-avant (telle que par exemple, la modification du document ou son résumé) nécessite l'autorisation préalable et expresse des auteurs ou de leurs ayants droit.

UNIVERSITY OF LIÈGE

Faculty of Applied Sciences

Experimental and numerical investigations of the VIV-galloping instability of a bluff body

---

Andrea AMBROSIO

In partial fulfillment of the requirements for a
Master’s degree in Aerospace Engineering

Supervisor: Thomas Andrianne

Academic year 2024-2025

Abstract

While VIV and galloping are well investigated separately, their coupled dynamics remain poorly understood. Experimental tests were hence conducted on a square-section cylinder in a wind tunnel to study their interaction at low Scruton numbers. The experimental results were compared to a numerical model that combines both phenomena, making use of the quasi-steady galloping theory and an unsteady fluctuating force. The goal was to assess the model's capability to capture both steady-state and transient responses across a range of reduced velocities.

The amplitudes of oscillations were overestimated close the critical VIV velocity but good agreement was observed between the model and experimental data at higher reduced velocities. In general, the model captured the dominant mechanisms in post-critical flow regimes, while showing limitations near the lock-in region. Regarding the transient behaviour and the build up of oscillations from rest, the model predicted the correct trend for varying airspeed and amplitude but the amplitude-dependent damping ratios were significantly underestimated. The transient trend was associated with the appearance of an even harmonic above a certain amplitude of motion. The numerical excitation force appeared to be overestimated compared to experimental measurements and the discrepancies of the model were attributed to the modeling of the unsteady aerodynamic force.

Overall, this work helps to better understand how VIV and galloping interact and how well a simple model can capture that behavior. The results showed where the model agrees with experiments and where it needs improvement.

Acknowledgements

First of all, I would like to express my deepest thanks to my supervior M. Thomas Andrianne for his support, guidance and availability throughout this research and for providing the necessary resources to make this work possible.

Then, special thanks goes to Edouard Verstraelen, in charge of the wind tunnel, for his insights, help and technical support regarding the experimental aspects of my work.

Another thanks goes to the technician Antoine for his assistance with the experimental setup and to the PhD candidate Simon Dehareng for taking the time to explain and show me the operation of the wind tunnel.

Finally, as this work concludes my engineering studies, I would like to thank my family and friends for their ongoing support, along with anyone who has helped me in this journey.

Contents

Nomenclature

Acronyms

DOF	Degree Of Freedom
LCO	Limit Cycle Oscillation
VIV	Vortex-Induced vibrations

Symbols

α	Angle of attack [rad]
δ	Logarithm decrement [-]
ν	Nondimensional wind speed [-]
ω_0	Natural circular frequency [rad s^{-1}]
ρ	Air density [kg m^{-3}]
τ	Reduced time [-]
ζ	Damping ratio [-]
a_g	Galloping stability parameter [-]
c	Structural viscous damping coefficient [N s m^{-1}]
C_{F_y}	Transverse force coefficient [-]
f_0	Structural natural frequency [Hz]
g	Acceleration of gravity [m s^{-2}]
h	Transverse length of the oscillating mass [m]
K	Reduced frequency [-]
k	Stiffness coefficient [N m^{-1}]
l	Spanwise length of the square cylinder [m]
m	Oscillating mass [kg]
m^*	Mass parameter [-]
n	Mass ratio [-]
Re	Reynolds number [-]
Sc	Scruton number [-]
St	Strouhal number [-]
t	Time [s]
$U_{r,g}^{\omega}$	Critical galloping reduced velocity, defined with ω_0 [-]
U_r	Reduced velocity [-]
U_r^{ω}	Reduced velocity defined with ω_0 [-]
U_r^{VIV}	Critical reduced velocity for VIV [-]
$U_{\infty,g}$	Critical galloping velocity [m s^{-1}]
U_∞	Free-stream velocity [m s^{-1}]
$U_{r,g}$	Critical galloping reduced velocity [-]
Y	Reduced displacement [-]
y	Transverse displacement of the oscillating mass [m]

Chapter 1

Introduction

1.1 Motivation

The name “aeroelasticity” was first proposed by Roxbee Cox and Pugsley in the 1930s. It is the study of the interaction of aerodynamic, elastic and inertial forces and encompasses several fields that can be visualized using Collar’s triangle (see Figure 1.1). Each of them adresses several aspects. Flight dynamics is concerned with gusts, loading problems, stability and control. Structural dynamics concerns general mechanical vibrations and impacts. Finally, static aeroelasticity studies control reversal and divergence. Combinig all of these aspects leads to dynamic aeroelasticity, which focuses on how unsteady aerodynamic forces interact with a flexible structure in motion and how that interaction can lead to dynamic behaviors like flutter or limit cycle oscillations.

Any aeroelastic problem involves the interaction between the structural dynamics of a system and the aerodynamic forces acting on it. The structure’s motion depends on its mass, stiffness, and damping properties, while the aerodynamic forces vary with the flow velocity and the structure’s displacement and velocity. Depending on the phenomenon, a model for the aerodynamic force is employed, which leads to airspeed-dependent stiffness and damping terms that lead to a dynamic system whose stability and response vary with flow conditions. This can result in behaviors such as flutter, where a dynamic instability arises from the interaction of structural modes; or limit cycle oscillations, where nonlinear effects stabilize otherwise unstable responses into periodic motion.

Aeroelastic phenomena have hence been studied for decades now, starting with aircrafts problems encountered. Over time, these studies expanded into the field of wind engineering, which examines the influence of wind on various structures such as buildings and bridges. Notably, the galloping phenomenon was first observed in 1930 called “dancing vibrations” of iced transmission lines which vibrated at about 1 Hz and up to 3 meters of amplitude. This early observation highlighted the potential severity of wind-induced effects on slender structures. Then, the famous event of the collapse of Tacoma Narrows bridge due to the interaction between torsional galloping and Vortex-Induced vibrations (VIV) marked a starting point in more profound studies of wind-excited structures.

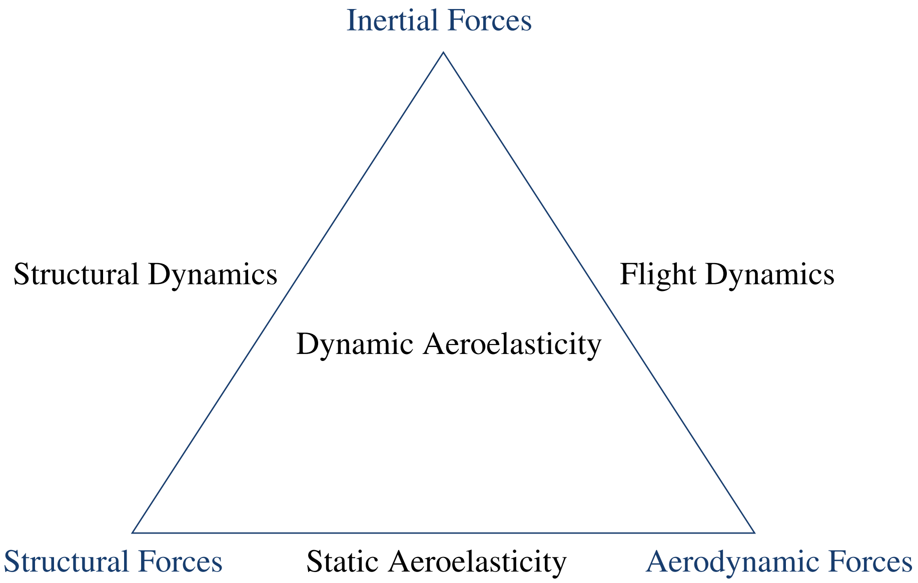

Figure 1.1: Representation of Collar's triangle [2].

This work will focus on two phenomena, VIV and galloping, that occur only for bluff bodies which are defined as solid objects whose wake size is comparable to their width. Due to their geometry, they create flow separation and the formation of turbulent wake regions when exposed to a fluid like air or water.

In general, VIV can occur for bridges, chimneys, buildings, risers in offshore platforms or heat exchangers. It is a critical consideration because the relatively small amplitudes of vibrations can lead to fatigue failure over time and increased maintenance needs. On the other hand, galloping occurs for slender bluff bodies with non-symmetric cross sections such as high-rise buildings and bridges. It is also a concern in structures exposed to wind since it produces large-amplitude oscillations, leading to serious structural and operational consequences.

The main goal of this work is to study the interaction of VIV and galloping. Indeed, when structural damping is low, these two phenomena can combine and produce high amplitudes of vibrations that cannot be predicted by both theories separately. As reported by Paidoussis et al. [33], probably the earliest example was reported in 1960 by Scruton [36], when he initially observed that the oscillatory response of a square-section cylinder exhibited distinct behaviors depending on the flow velocity. At low flow speed, the vibrations were driven by VIV, while at higher velocities, an instability due to galloping occurred. Between these two regimes, a stable region was present. However, when structural damping was reduced, the clear distinction between VIV and galloping responses disappeared. Instead, one combined instability was observed. To this day, the phenomenon is still not well understood, even though it has received great attention from researchers.

1.2 Methodology and overview

The focus will remain on the case of a square cylinder, which will be studied through experimental tests conducted in the wind tunnel facility of the University of Liège. Although quite academic, the square cross-section is representative of many real-world applications, as it is commonly found in building elements, signposts, bridges, and chimneys. These experiments aim to characterize the coupled VIV-galloping behavior under controlled conditions and to gather data. Indeed, the experimental results will then be compared to the predictions of a numerical model in order to evaluate the model's accuracy, identify its limitations, and determine how predictive capabilities can be improved.

Concerning the structure of this work, it first goes through the theoretical aspects of bluff body aeroelasticity and aerodynamics to build a strong foundation for the understanding of the combined effects of VIV and galloping.

Then, the mechanisms that are responsible for both phenomena sperately are described mathematically and physically. Within this theoretical part, note that some of the described aspects are illustrated using experimental tests conducted during the realisation of this work on a scaled model of the Vialta footbridge [10]. Their use initially intented to remain dissociated from this work but it turned out that it enabled to have a better understanding of the aeroelastic phenomena that will be studied and, more importantly, allowed the validation of the modal parameters extraction process through namely the determination of the natural frequency of the structure and the structural damping ratio.

Numerical models are then presented, first individually for VIV and galloping, followed by a model combining both. After that, the experimental setup used for the wind tunnel tests is described. Experimental methods for determining structural damping, vital in this work, are also discussed. Then, a first part of the experimental results is presented without the numerical aspect in order to focus purely on the behavior observed.

A comparison between the experimental and numerical results is then conducted to verify the accuracy of the model in terms of the amplitudes of vibration and the modeling of the aerodynamic excitation. Time-domain and frequency-domain analyses are used for a complete characterization of the system's dynamic response, allowing for a detailed understanding of both steady-state oscillations and transient behavior.

Finally, the main conclusions of the study are presented, and limitations of the present work are adressed. Potential directions for future research are proposed. In particular, exploring the influence of additional parameters not assessed in this work could provide valuable insights and contribute to a more comprehensive understanding of the phenomenon as a whole.

Concerning the use of artificial intelligence, generative AI tools were only used to assist in brainstorming ideas, coding issues, searching information similarly to a search engine, summarize research articles and provide alternative phrasings, following the policy of the university of Liège on the use of generative artificial intelligence in academic work [40].

Chapter 2

Bluff body aeroelasticity

This chapter introduces the concepts that are adressed in this work. Particularly, bluff body aerodynamics are described and the two aeroelastic instabilities vortex-induced vibrations and galloping, whose interaction is the topic of this work, are explained. Numerical models are then described for both of them as well as one combining the two phenomena.

2.1 The Navier-Stokes equations

First of all, fluid mechanics are ruled by the Navier-Stokes equations. They are composed of the conservation of mass, momemtum and energy. The discussion here will only involve the conservation of momemtum. Particularly, the incompressible flow assumption will be used and is possible thanks to the flow speed which remains much lower than the speed of sound (Mach number lower than 0.3) such that the density is assumed to be constant. The conservation of momemtum can thus be written for an incompressible flow in nondimensional form as

$$St\frac{\partial \bar{\mathbf{U}}}{\partial \bar{t}} + \left(\bar{\mathbf{U}} \cdot \nabla\right) \bar{\mathbf{U}} = -\nabla \bar{p} + \frac{1}{Re}\Delta \bar{\mathbf{U}} + \frac{1}{Fr^2}\bar{\mathbf{f}}_{\mathbf{e}} \tag{2.1}$$

where $\bar{\mathbf{U}}$, $\bar{t}$, $\bar{p}$ and $\bar{\mathbf{f}}_{\mathbf{e}}$ are respectively the nondimensional airspeed, time, pressure and vector of external volume forces. Important non-dimensional numbers are present this equation. St is the Strouhal number, Re is the Reynolds number and Fr is the Froude number, respectively given by

$$St = \frac{L}{UT} \qquad Re = \frac{\rho U L}{\mu} \qquad Fr = \frac{U}{\sqrt{Lg}} \tag{2.2}$$

with μ the dynamic viscosity of the fluid. Concerning the Strouhal number, it will play an important role throughout this study. Indeed, it can be seen that it multiplies the time derivative of the flow velocity in equation (2.1). Therefore, it quantifies how unsteady the flow is. Section 2.2.1 explains in more detail the use of this number.

Then, the Reynolds number represents the ratio between inertial and viscous forces. Hence, it is the ratio between momemtum convection and diffusion. The key aspect is that its value characterizes the flow regime. For $Re < 2000$, the flow is laminar and viscous effects are predominant. Then, when $2000 < Re < 3000$, there is a transition zone to the turbulent regime ($Re > 3000$), where viscous effects become less important. In this work, the Reynolds number varies approximately from $2 \cdot 10^4$ to $6 \cdot 10^4$ corresponding thus to a turbulent flow.

Finally, the Froude number is the ratio of inertial and gravity forces. It is used primarily in hydraulics with two immiscible fluids and will not be particularly useful in this work.

2.2 Bluff body aerodynamics

Bluff bodies are defined as objects whose wake size is comparable to their height, as opposed to streamlined shapes that keep the flow attached like an airfoil at a small angle of attack. Bluff bodies, such as square cylinders, lead inexorably to flow separation because of their geometry.

2.2.1 The vortex shedding process

The vortex street behind a bluff body is called "Karman vortex street" after the work of Theodore von Karman [41] in 1911 where he studied the formation of vortices periodically shed behind a bluff body (see Figure 2.1). The vortices are shed alternatively from one side of the body to the other and it occurs at a particular frequency f_{vs}. On top of that, f_{vs} increases linearly with the airspeed, following the Strouhal law

$$St = \frac{f_{vs} h}{U_\infty} \rightarrow f_{vs} = \frac{St}{h} U_\infty \tag{2.3}$$

where h is the length of the section perpendicular to the flow and U_∞ is the freestream velocity. Note that St depends on the shape of the section and varies with the Reynolds number although it can be considered constant in a certain Re range (see section 2.3.1). At the origin of the vortex shedding process lies a shear layer instability, where there are strong gradients and which is actually an inviscid phenomenon. Vorticity is continuously produced in the wake such that the flow speed is much larger outside than inside the wake.

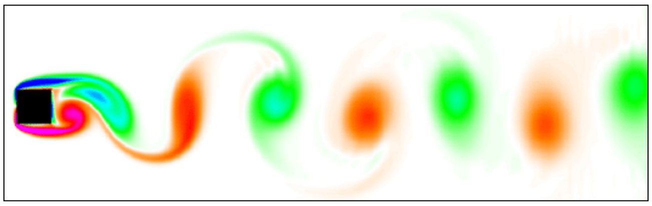

Figure 2.1: Representation of the vortex street behind a bluff body such as a square section [21].

Note that the Strouhal number will be assumed constant here while in reality it varies with the

Reynolds number. Figure 2.2 shows the effect of the Reynolds number on St for a square section, obtained through numerical and experimental data [25]. The retained value for the Reynolds range $10^4 - 10^5$ is $St \approx 0.13$ and will be the one used in this work.

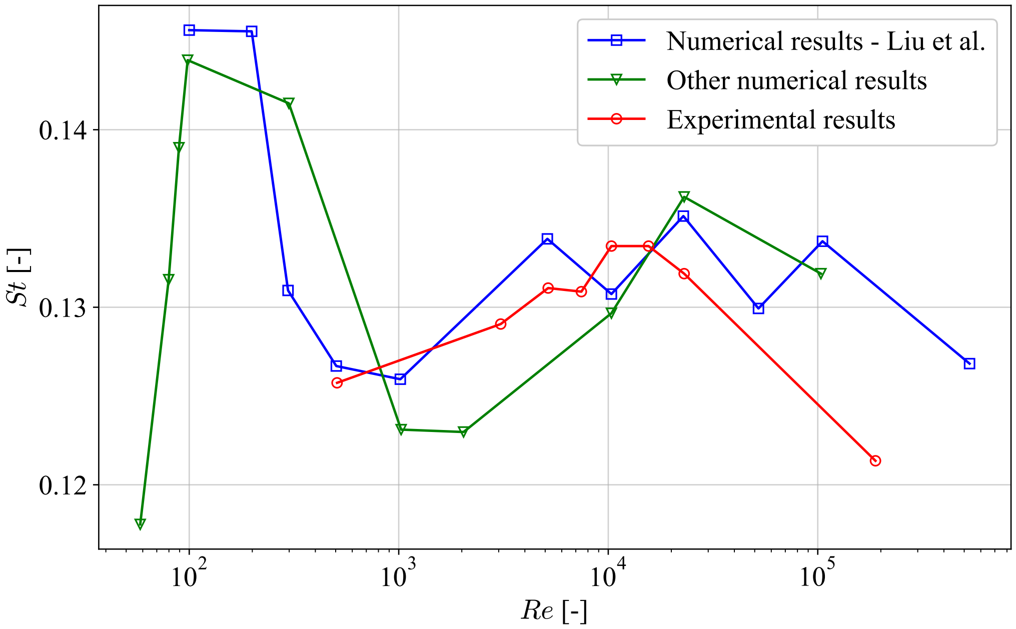

Figure 2.2: Reynolds effect on the Strouhal number for a square cylinder, as reported by Liu et al. [25]. Other numerical results are presented [44] [1] as well as experimental measurements[43] [22] [35].

The vortices behind a bluff body are also shed according to multiple modes, as reported originally by Strouhal [9]. He observed a low-speed mode due to a laminar wake instability, followed by a high-speed mode. The evolution of the Strouhal number as a function of the Reynolds number was also studied and there were two discontinuities observed. First, when transitioning from one mode to the other and then later for higher Reynolds numbers. It shows how the vortex shedding pattern influences the development of unsteady aerodynamic forces acting on the body.

2.2.2 The quasi-steady assumption

In order to model a complex phenomenon, assumptions have to be made in order to simplify the problem and enable understanding of the dynamic at play. One of the most important assumptions in this work concerns the quasi-steady assumption, which considers that the motion of the structure is slow compared to the motion of the fluid.

Let's first define the reduced velocity U_r as

$$U_r = \frac{U_\infty}{f_0 h} \tag{2.4}$$

where one finds the free-stream velocity U_∞, the natural frequency of the structure f_0 and the distance h, taken to be the side length of the square section perpendicular to the flow. This is thus a nondimensional velocity. It can be re-written using the period of motion $T_0 = 1/f_0$ as

$$U_r = U_\infty \frac{T_0}{h} = \frac{U_\infty}{U_{motion}} \tag{2.5}$$

Therefore, if U_r is small, $U_{motion} \gg U_\infty$ and the structure vibrates at a much higher speed than the wind speed. In that case, the quasi-steady assumption does not hold, as the phenomenon is highly unsteady. In contrast, if U_r is large, $U_{motion} \ll U_\infty$ such that the structure vibrates slowly compared to the air velocity. The flow has time to adapt to the movement of the oscillating system. In this case, the quasi-steady assumption is verified.

It is worth noting that some authors adopt a different definition for the reduced velocity, by using $\omega_0 = 2\pi f_0$ instead of f_0, and that will be noted U_r^ω such that

$$U_r^\omega = \frac{U_\infty}{\omega_0 h} = \frac{1}{2\pi}\frac{U_\infty}{f_0 h} \tag{2.6}$$

$$= \frac{1}{2\pi} U_r \tag{2.7}$$

In this work, the first definition will be used more nonetheless since it is easier to talk in terms of frequency than pulsation. Similarly, the reduced frequency K is defined as

$$K = \frac{\omega_0 h}{U_\infty} \tag{2.8}$$

such that it is in fact the inverse of U_r^ω. Using analogous reasoning, one finds that low values of K are associated to the quasi-steady assumption while large values of K treat unsteady phenomena.

However, this brings a new question: how large should the reduced velocity be for this assumption to be valid ? There is no real consensus for a minimum value of the reduced velocity. Early on, Fung [14] proposed $U_r > 10$ by considering that “any disturbance experienced by the oscillating body at a certain point of its motion must be swept downstream sufficiently far, by the time the body comes back to that same point, of the disturbance to no longer affect the flow around the body”. Then, Blevins [7] considered that the frequency of the shed vortices must be at least twice as large as the oscillating frequency, which leads to $U_r > 2/St$. Nakamura and Mizota [39] consider that the reduced velocity should be at least twice the critical VIV velocity, which is basically the same condition (see section 2.3.1 for its definition). More recently, Carasalle [27] reported that $U_r > 20$ is generally accepted for the quasi-steady assumption to be valid. Therefore, for reduced velocities below 10-15, one can expect the quasi-steady to not be as accurate due to the unsteady nature of the flow.

2.3 Instabilities

The two separate aeroelastic phenomena, whose interaction is studied in this work, are now described physically and mathematically in order to introduce their mechanisms and provide a basis for understanding their combined effects.

2.3.1 Vortex-Induced vibrations

The first aeroselastic phenomenon of interest is called vortex-induced vibrations (VIV), which usually occurs at low speed and thus low reduced velocities. The problem with VIV is that it starts at low velocities and has small oscillation amplitudes, so it creates fatigue in the materials of the structure.

Physical origin

VIV is a frequency-matching aeroelastic phenomenon, occurring when the frequency at which vortices are shed behind a bluff body f_{vs} becomes equal to the structural natural frequency f_s^0. Indeed, the periodic shedding of the vortices in the wake is able to excite the system at the same frequency and make it enter resonance.

It is thus an unsteady phenomenon occuring generally at low reduced velocities. The quasi-steady assumption can not be employed as will be discussed in the modelling section.

Critical VIV velocity

The critical airspeed at which VIV starts can be computed by considering the frequency matching between f_0 and f_{vs} hence

$$f_{vs} = \frac{St}{h} U_\infty = f_0 \tag{2.9}$$

$$\Leftrightarrow U_{VIV} = \frac{f_0 h}{St} \tag{2.10}$$

and the critical reduced velocity for VIV if therefore given by

$$U_r^{VIV} = \frac{U_{VIV}}{f_0 h} = \frac{1}{St} \tag{2.11}$$

It has to be mentionned that U_r^{VIV} does not depend on damping at all hence, for several damping values, VIV will begin at the same wind speed. The critical velocity is thus rather straightforward to determine since it is based on the Strouhal number, which is well known for usual cross sections such as rectangular cross sections with a certain side ratio as in Figure 2.3. If the section is more exotic, it can be determined experimentally by measuring the velocity in the wake for multiple wind speeds, computing the main frequency component to get f_{vs} and retrieving St through the slope of the Strouhal law. If the dimensional velocity is required, only the transverse length of the cross section and the natural frequency of the structure are needed.

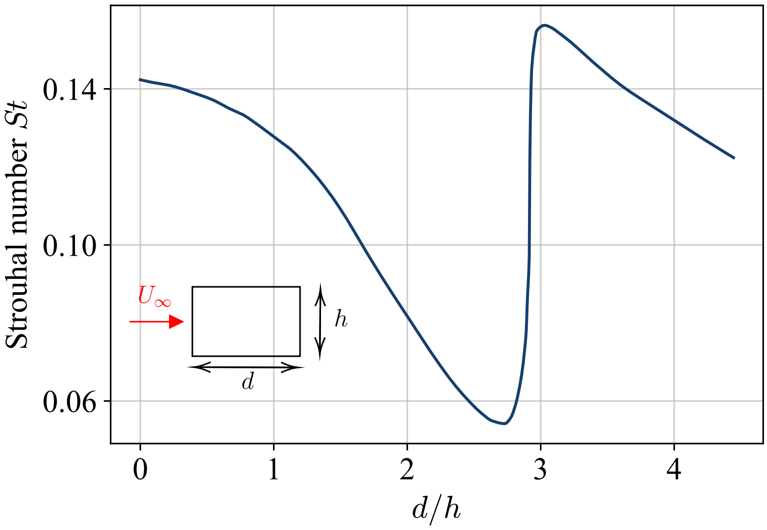

Figure 2.3: Effect of the side ratio d/h of rectangular cross sections on the Strouhal number [17].

When increasing the wind velocity after the critical airspeed, the wake is first captured by the oscillations of the structure such that in a certain range of velocities, called the lock-in range, the vortex shedding frequency is constant and remains equal to the natural frequency of the structure. As a result, the amplitude increases since the vortices still excite the structure at the same frequency. The amplitude reaches a maximum after which it goes back to zero because at some point the wake is no more captured by the vibrations and the vortex shedding frequency is no more equal to f_0. Hence, f_{vs} goes back to follow the Strouhal law.

The typical response amplitude for VIV has a clutch shape as can be seen in Figure 2.4, corresponding to amplitudes measured experimentally for the footbridge described in the introduction and where the critical VIV velocity is indicated. It can be seen that this critical velocity is well predicted, and adding damping decreases the maximum amplitude and the lock-in range.

Additionally, the range of velocities where the amplitude is different from zero decreases as structural damping increases. As a result, there are two key quantities to characterize vortex-induced vibrations: the maximum amplitude of motion and the lock-in range. Increasing structural damping will decrease the maximum amplitude reached by the structure and also decrease the lock-in range up to a point where VIV is completely suppressed.

One can thus also realize that the velocity at which VIV starts is rather simple to determine, as opposed to the maximum amplitude and the lock-in range, which require experimental testing and/or appropriate mathematical modeling.

Hence, VIV can be attenuated by increasing damping. Note that in practice, depending on the experimental setup, adding damping may add stiffness to the system, which increases slightly f_0 and

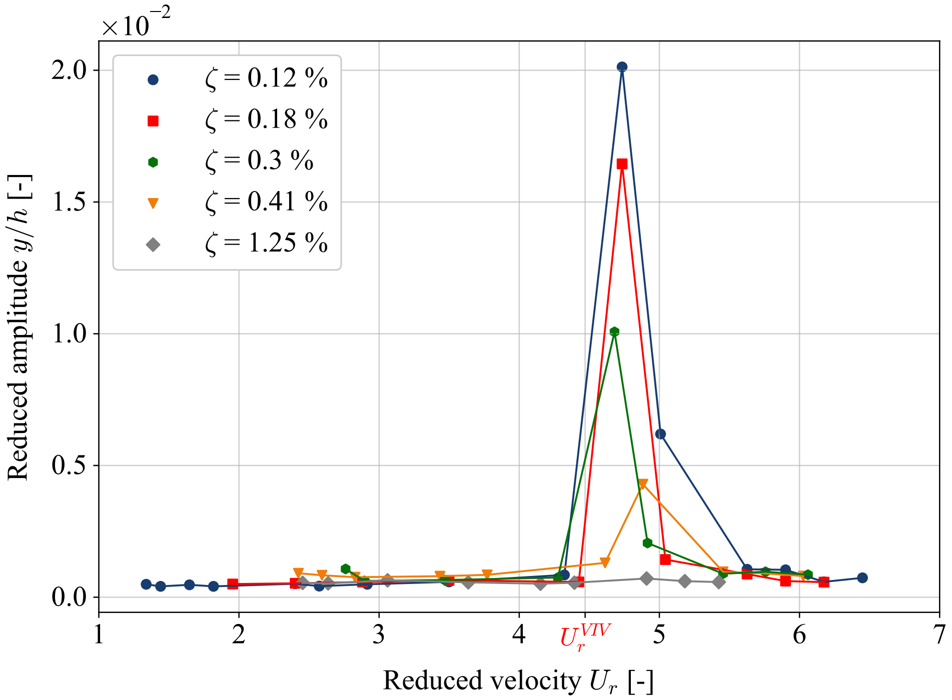

Figure 2.4: Reduced amplitudes of VIV vibration obtained for the footbridge at different structural dampings levels.

thus the wind speed required for frequency matching. Other than through damping, eliminating VIV can be done, for instance, by changing the shape of the structure to avoid the vortex shedding process to excite the structure. An example would be to use a splitter plate placed downstream of the body. It is unconnected and stationary, and enables breaking the vortices [33]. However, this is often not possible. One could also consider adding stiffness to increase the natural frequency and delay the start of VIV.

As a final remark, one could note that since f_{vs} increases linearly with the wind speed, frequency matching can occur at multiple airspeeds if the structure has multiple transverse modes of vibration at higher frequencies, though it will not play a role in this work.

Nondimensional parameters

Based on what has been explained concerning VIV, it can be determined on which nondimensional variables its characterization can be based on.

The reduced amplitude y/h and the lock-in range depend on the geometry of the system namely the ratio of the transverse side length to the spanwise length of the structure h/l. There is also obviously the reduced velocity and the Reynolds number that have an effect on the shedding process. Then, as already mentionned, damping plays an important role through the damping ratio and finally the last nondimensional variable is the mass parameter m^* which is defined as the ratio of the mass of the structure per unit length to the fluid mass per unit length m_f occuping the same volume. For a square cylinder, one has thus $m_f = \rho h^2$ such that $m^* = \frac{m}{\rho h^2 l}$. It represents the susceptibility of the system to flow induced vibrations.

Hence, one can write generally that the amplitude of motion and what characterizes the lock-in range are a function of

$$\left[\frac{y}{h}, f_s, f_{vs}\right] = F\left(\frac{h}{l}, U_r, Re, m^*, \zeta\right) \tag{2.12}$$

which expresses all parameters of interest in terms of nondimensional parameters. It is worth mentionning that the mass parameter and the damping ratio can be combined into one nondimensional number, called the Scruton number Sc, which is defined as

$$Sc = 4\pi m^* \zeta \tag{2.13}$$

It is thus a measure of structural damping and mass of the structure that will be used extensively for experimental tests since it combines both informations.

2.3.2 Galloping

The second aeroelastic phenomenon studied here is called galloping and usually occurs at high reduced velocities. This instability results from the non-symmetrical shape of the structure such as a square, hence a circular cylinder can never undergo galloping. Unlike VIV, the quasi-steady theory can be used. The focus of this work is on transverse galloping interacting with VIV.

Mechanism

During oscillations, the square has at some point a downward velocity component $\dot{y}$ which is equivalent to a stationary square with an upward wind. Therefore, instead of being subjected to U_∞, the structure "sees" a relative velocity V_{rel} at a certain angle of attack α. The quasi-steady theory assumes that a cylinder moving at a downward speed $\dot{y}$ is equivalent to a stationary cylinder being subjected to V_{rel} at an angle of attack $\alpha = \tan^{-1}\left(\frac{\dot{y}}{U_\infty}\right)$ (see Figure 2.5).

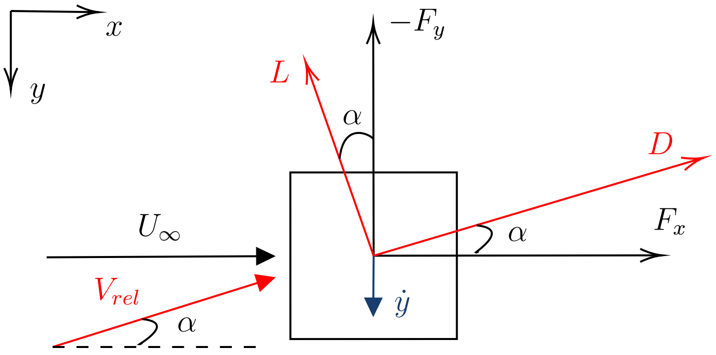

Figure 2.5: Schematic of the relative velocity seen by the square cylinder due to the downward velocity $\dot{y}$ and the resulting forces. F_y and F_x denote respectively the transverse and axial forces.

As usual, the lift and drag forces are expressed

$$L = \frac{1}{2}\rho U_\infty^2 hlC_L \qquad D = \frac{1}{2}\rho U_\infty^2 hlC_D \tag{2.14}$$

where l is the spanwise length of the square cylinder. For galloping, the interest lies in the transverse force F_y that is linked to L and D through

$$F_y = -L\cos\alpha - D\sin\alpha \tag{2.15}$$

The stability of the structure is determined by the sign of $\frac{dF_y}{d\alpha}$ i.e. the change in the transverse force due to a change in the angle of attack:

- If $\frac{dF_y}{d\alpha} < 0$, an increase in α (thus $\dot{y}$) leads to a decrease in F_y. The system is stable.
- If $\frac{dF_y}{d\alpha} > 0$, an increase in α leads to an increase in F_y. The system is unstable. The force increases with increasing velocity of motion and energy is transferred from the flow to the structure.

This instability condition can be reformulated by developing the derivative. Indeed, differentiating with respect to α gives

$$\frac{dF_y}{d\alpha} = \left(L - \frac{dD}{d\alpha}\right)\sin\alpha + \left(-\frac{dL}{d\alpha} - D\right)\cos\alpha \tag{2.16}$$

Then, using the expressions of the lift and drag forces and linearizing by using the fact that for a square section $C_L = 0$ and $\frac{dC_D}{d\alpha} \approx 0$ around 0° gives

$$\frac{dF_y}{d\alpha} = \frac{1}{2}\rho U_\infty^2 hl\left[\left(\cancel{C_L} - \cancel{\frac{dC_D}{d\alpha}}\right)\sin\alpha + \left(-\frac{dC_L}{d\alpha} - C_D\right)\cos\alpha\right] \tag{2.17}$$

$$= -\frac{1}{2}\rho U_\infty^2 hl\left(\frac{dC_L}{d\alpha} + C_D\right)\underbrace{\cos\alpha}_{\approx 1} \tag{2.18}$$

$$= -\frac{1}{2}\rho U_\infty^2 hl\left(\frac{dC_L}{d\alpha} + C_D\right) \tag{2.19}$$

Finally, the so-called Den Hartog's criterion [32] can be written as

$$\frac{dF_y}{d\alpha} > 0 \quad \Leftrightarrow \quad \frac{dC_L}{d\alpha} + C_D < 0 \tag{2.20}$$

The two expressions are therefore completely equivalent. Den Hartog's criterion enables however to determine the stability of the structure based on usual aerodynamic quantities, namely the slope of the lift coefficient and the drag coefficient [38]. Note that it is common to define the critical galloping factor (also called the galloping stability parameter) a_g as

$$a_g = -\left(\frac{dC_L}{d\alpha} + C_D\right)\bigg|_{\alpha=0^\circ} \tag{2.21}$$

such that the instability condition of equation (2.20) becomes $a_g > 0$ around $\alpha = 0^\circ$.

Finally, looking back at equation (2.19), it appears that since the transverse force coefficient is defined as

$$C_{F_y} = \frac{F_y}{\frac{1}{2}\rho U_\infty^2 hl} \tag{2.22}$$

then a_g is simply the slope of $C_{F_y}(\alpha)$ at $\alpha = 0^\circ$. Galloping will thus occur if the slope of $C_{F_y}(\alpha)$ at the origin is positive. It is worth mentioning that, in general, for rectangular bluff bodies, this condition, which is the same as Den Hartog's criterion, is a sufficient but not necessary condition for galloping. If it is verified, galloping will occur, but galloping can occur even if it is not satisfied. This results from the fact that the equations were linearized as explained by Novak [30]. In any case, it will later be shown that, of course, for a square section, one has $a_g > 0$.

Critical galloping velocity

The focus will be now to understand what causes galloping and to predict the velocity at which it will occur through a linear approach. To this end, a one degree of freedom system excited by the transverse force is considered (Figure 2.6) with linear spring and viscous damping structural elements.

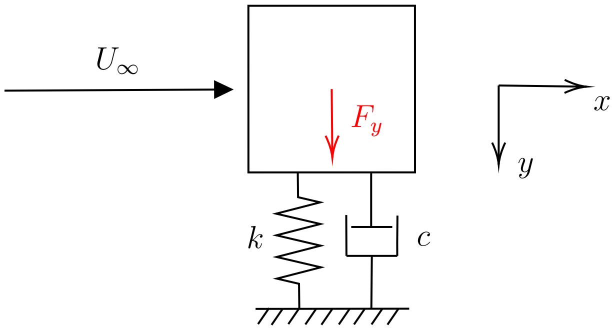

Figure 2.6: Square cylinder modelled as a 1-DOF system excited by the transverse force F_y due to the wind speed U_∞.

and whose equation of motion is simply

$$m\ddot{y} + c\dot{y} + ky = F_y \tag{2.23}$$

Using the expression of F_y and assuming that α is small gives succesively

$$m\ddot{y} + c\dot{y} + ky = -L\cos\alpha - D\sin\alpha \tag{2.24}$$

$$\approx -L - D\alpha \tag{2.25}$$

$$\approx -\left(L_0 + \left.\frac{dL}{d\alpha}\right|_{\alpha=0^\circ}\alpha\right) - \left(D_0 + \left.\frac{dD}{d\alpha}\right|_{\alpha=0^\circ}\alpha\right)\alpha \tag{2.26}$$

$$\approx -L_0 - \left(\left.\frac{dL}{d\alpha}\right|_{\alpha=0^\circ} + D_0\right)\alpha \tag{2.27}$$

$$\approx -L_0 - \left(\left.\frac{dL}{d\alpha}\right|_{\alpha=0^\circ} + D_0\right)\frac{\dot{y}}{U_\infty} \tag{2.28}$$

where second-order terms have been neglected and $\frac{dD}{d\alpha}\big|_{\alpha=0^\circ} \approx 0$. A Taylor expansion has also been used for both L and D around 0°. In the next part of this derivation, to avoid heavy notations, the evalutaion bar $|_{\alpha=0^\circ}$ and the subscript 0 are discarded but one has to keep in mind that the lift slope and the drag coefficient are evaluated at $\alpha = 0^\circ$ since the equations were linearized around that point.

Continuing, since the lift force for a square cylinder around 0° angle of attack $L_0 \approx 0$ and, realising that the right-hand side of the equation is in fact a damping term because it is proportionnal to $\dot{y}$, one can group the terms as

$$m\ddot{y} + \left[c + \left(\frac{dL}{d\alpha} + D\right)\frac{1}{U_\infty}\right]\dot{y} + ky = 0 \tag{2.29}$$

$$\Leftrightarrow m\ddot{y} + \left[c + \left(\frac{dC_L}{d\alpha} + C_D\right)\frac{1}{2}\rho U_\infty hl\right]\dot{y} + ky = 0 \tag{2.30}$$

Finally, re-writing in terms of modal parameters upon dividing by m yields

$$\ddot{y} + 2\omega_0\left[\zeta + \left(\frac{dC_L}{d\alpha} + C_D\right)\frac{\rho U_\infty hl}{4m\omega_0}\right]\dot{y} + \omega_0^2 y = 0 \tag{2.31}$$

This is an important equation as it appears that the system possesses structural damping and, added to it, aerodynamic damping which depends on the airspeed. Total damping can therefore become equal to zero when aerodynamic damping is negative enough. This gives a condition for the critical galloping velocity $U_{\infty,g}$ since it is the wind speed for which total damping vanishes, hence

$$U_{\infty,g} = -\frac{4m\zeta\omega_0}{\rho hl\left(\frac{dC_L}{d\alpha} + C_D\right)} \tag{2.32}$$

Attention should be paid to the minus sign in front of the fraction, indicating that in order for this critical speed to have a physical meaning, it requires $\frac{dC_L}{d\alpha} + C_D < 0$, such that Den Hartog's criterion is recovered. The critical galloping reduced velocity $U_{r,g}$ is given by

$$U_{r,g} = -\frac{4m\zeta\omega_0}{\rho h^2 l\left(\frac{dC_L}{d\alpha} + C_D\right)\frac{\omega_0}{2\pi}} \tag{2.33}$$

$$= -\frac{2 \cdot 2\pi\zeta}{n\left(\frac{dC_L}{d\alpha} + C_D\right)} \tag{2.34}$$

where the mass ratio is defined as $n = \frac{\rho h^2 l}{2m}$. It is important to note that this critical speed is directly proportional to the structural damping ratio. Therefore, if ζ is doubled, so is $U_{r,g}$. As a result, galloping is a damping-controlled instability since it can be pushed away by increasing structural damping. Note that $U_{r,g}$ can also be increased by decreasing n, which basically means increasing the mass of the structure.

Later, the velocity at which galloping starts will be compared to this quasi-steady for low structural damping. Indeed, it is expected to be less precise for lower reduced velocities where the quasi-steadiness of the flow can not be assumed anymore.

2.4 Models

After having a fundamental understanding of the mechanisms at play, models for the separated VIV and galloping phenomena are presented in this chapter. Then, a model combining the two previous ones is introduced with a discussion on the input parameters that are required for appropriate modeling.

2.4.1 VIV

The VIV phenomena can be modeled using different types of models. The focus will be on the most advanced type, a wake oscillator introduced by Hartlen and Currie [34]. It was originally proposed for circular cylinders but is adapted here to the square section.

Among the types of models, the first one considers a simple mechanical system excited by the lift force $L(t)$. For this type of model, the exciting force depends on the airspeed through the forcing frequency of a sinusoidal lift force via the Strouhal law. Then, one can try to improve this model to obtain the second type of model where the lift force is similar as before except that its amplitude depends now on the amplitude of vibration. Finally, the wake oscillator type of model considers that the lift force is the result of wake dynamics, itself influenced by the structural motion. One has to therefore consider the coupling of two systems: the cylinder and the wake.

For the cylinder, the starting point is a mechanical system excited by the unsteady lift force due to vortex excitation C_v

$$m\ddot{y} + c\dot{y} + ky = \frac{1}{2}C_v \rho U_\infty^2 hl \tag{2.35}$$

where l is the longitudinal length of the square cylinder. The equation of motion can be adimensionnalized by defining the reduced displacement $Y = y/h$, the reduced time $\tau = \omega_0 t$ and the mass ratio

$n = \frac{\rho h^2 l}{2m}$. The derivative with respect to time has to be adapted using the chain rule

$$\frac{d}{dt} = \frac{d\tau}{dt}\frac{d}{d\tau} = \omega_0 \frac{d}{d\tau} \tag{2.36}$$

In the following, the derivative with respect to τ is noted $.''$. The nondimensional equation of motion of the cylinder is thus given by

$$Y'' + 2\zeta Y' + Y = n(U_r^\omega)^2 C_v \tag{2.37}$$

The challenge is the approriate modelling of the excitation C_v. The quasi-steady assumption is not valid as the velocity of motion of the structure is comparable to the wind speed. Nonetheless, C_v should first include the periodic nature of the excitation. Then, from a stationary cylinder, the excitation is self-starting and self-limiting with limiting amplitude C_{Y_0}. The nonlinear oscillator equation for C_v is thus written as

$$C_v'' + \nu^2 C_v = a(\nu)\nu \left(C_v' - \frac{4}{3C_{Y_0}^2 \nu^2}(C_v')^3 \right) + D(\nu) Y' \tag{2.38}$$

where ν is the ratio between the reduced velocity U_r and the critical reduced velocity for VIV, or $\nu = U_r / U_{VIV}^r$. This is a Rayleigh equation and captures all the required features. Note that a van der Pol equation is also possible as shown by other wake oscillator models [29] [15]. The obtained equation contains three free parameters namely $a(\nu)$, C_{Y_0} and $D(\nu)$ that have to be determined through experimental tests and will be discussed later on for the combined model of VIV and galloping. The two equations are thus coupled through the C_v and Y' terms.

2.4.2 Galloping

As already mentionned before, modelling galloping is possible thanks to the quasi-steady assumption since it occurs generally at high reduced velocities. So far, only the critical airspeed for galloping could be computed on the basis of a linear approach. However, now, the focus will be on the resulting amplitude of motion, which will need the inclusion of nonlinear terms to capture the phenomenon.

For a square cylinder, Parkinson and Smith [42] obtained an S-shaped curve called the universal galloping curve. Starting from the equation of motion of a linear elastic system

$$m\ddot{y} + c\dot{y} + ky = \frac{1}{2} C_{F_y} \rho U_\infty^2 hl \tag{2.39}$$

where l is the longitudinal length of the square cylinder and the quasi-steady assumption can be used for the transverse force coefficient C_{F_y}. From static wind tunnel testing, it can be measured as a function of the angle of attack $\alpha \approx \tan(\alpha) = \frac{\dot{y}}{U_\infty}$. Therefore, C_{F_y} can be approximated by a polynomial in $\dot{y}/U_\infty$ with odd powers only due to the geometrical symmetry. They used a seventh degree polynomial to account for the five inflection points observed experimentally.

As a result, all terms are now included and not just the linear term as before. C_{F_y} is thus expressed as

$$C_{F_y} = A\left(\frac{\dot{y}}{U_\infty}\right) - B\left(\frac{\dot{y}}{U_\infty}\right)^3 + C\left(\frac{\dot{y}}{U_\infty}\right)^5 - D\left(\frac{\dot{y}}{U_\infty}\right)^7 \tag{2.40}$$

Attention has to be paid to the minus signs in front of the third and seventh order terms such that all coefficients are positive. Their reproduced data for $C_{F,y}$ is depicted in Figure 2.7. One can observe the positive slope at the origin, responsible for galloping. Note that there are two inflection points, near $\alpha = 7°$ and $\alpha = 11°$, which will be relevant later on.

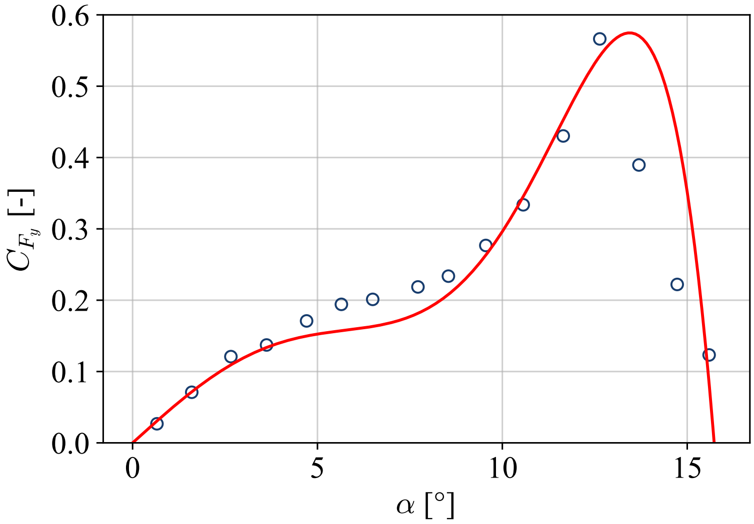

Figure 2.7: Transverse force coefficient as a function of the angle of attack. ○ Experimental data and —— fitting polynomial with A = 2.69, B = 168, C = 6270 and D = 59900. Reproduced from Parkison and Smith [42].

Then, the equation of motion is adimensionnalized as before and by dividing by kh, which yields

$$\frac{m}{k}\ddot{Y} + \frac{c}{k}\dot{Y} + Y = \frac{\rho U_\infty^2 l}{2k}\left[A\left(\frac{\dot{y}}{U_\infty}\right) - B\left(\frac{\dot{y}}{U_\infty}\right)^3 + C\left(\frac{\dot{y}}{U_\infty}\right)^5 - D\left(\frac{\dot{y}}{U_\infty}\right)^7\right] \tag{2.41}$$

After simple algebraic manipulations, the non-dimensional equation of motion is obtained

$$Y'' + 2\zeta Y' + Y = n\left[AU_r^\omega Y' - B\frac{1}{U_r^\omega}(Y')^3 + C\frac{1}{(U_r^\omega)^3}(Y')^5 - D\frac{1}{(U_r^\omega)^5}(Y')^7\right]$$

$$\Leftrightarrow Y'' + Y = nA\left[\left(U_r^\omega - \frac{2\zeta}{nA}\right)Y' - \left(\frac{B}{AU_r^\omega}\right)(Y')^3 + \left(\frac{C}{A(U_r^\omega)^3}\right)(Y')^5 - \left(\frac{D}{A(U_r^\omega)^5}\right)(Y')^7\right]$$

which is a second order nonlinear differential equation to solve for $Y(\tau)$. Parkinson and Smith used an asymptotic approach called the Krylov-Bogoliubov method to solve this equation. For the purposes of this work, the equation of motion will be integrated numerically using the Runge-Kutta algorithm.

Nevertheless, the critical galloping velocity appears in the equation as

$$U_{r,g}^{\omega} = \frac{2\zeta}{nA} \tag{2.42}$$

since it cancels out the damping term proportional to Y'. The linear result is therefore retrieved. Indeed, it is obviously equivalent to the one demonstrated previously in section 2.3.2 since they both rely on the quasi-steady theory. Note that the 2π factor of equation (2.34) comes from the different definition of the reduced velocity (using f_0 or ω_0). Moreover, it is clear that the polynomial coefficient A is none other than a_g itself and corresponds indeed to the linear slope of C_{F_y} around $\alpha = 0°$.

The solution $Y(\tau)$ is a sinusoidal signal that grows in amplitude until reaching Limit Cycle Oscillations (LCOs) which corresponds to periodic motion. As the wind speed increases, the steady-state amplitude also increases as energy transfer from the flow to the structure becomes larger. Solving this equation for multiple wind speeds enables to plot the dependence of the amplitude on the airspeed, which looks like a S shape for a square cylinder. An example is depicted in black in Figure 2.8, along with reproduced experimental data matching correctly. An important result is that when plotting the reduced amplitude Y in terms of the reduced velocity U_r^{ω}, both multiplied by the nondimensional factor $\frac{nA}{2\zeta}$, all experiments with different damping ratios and mass ratios collapse to a single curve hence the name “universal galloping curve”. The critical galloping velocity is therefore located at 1 on the horizontal axis, when $U_r^{\omega} = U_{r,g}^{\omega}$. Moreover, as U_r^{ω} tends to infinity, the amplitudes of motion become asymptotic, independently of ζ and n.

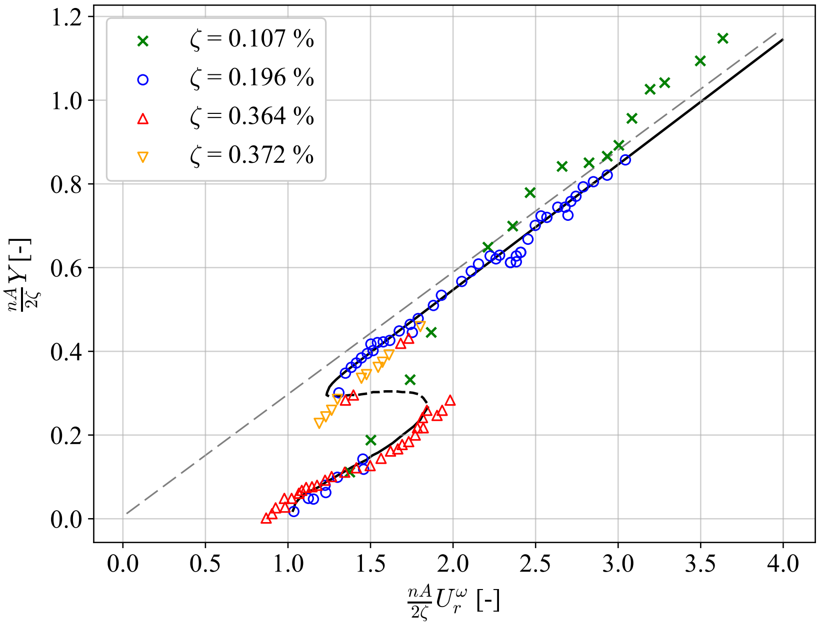

Figure 2.8: Amplitude-velocity characteristics of galloping of a square cylinder. Scattered results correspond to experimental data. —— Theoretical stable limit cycle, - - - - experimental unstable limit cycle and — — asymptotic limit cycle. Re ranges from $4 \cdot 10^3$ to $20 \cdot 10^3$, $n = 4.3 \cdot 10^{-4}$. Reproduced from Parkinson and Smith [42].

Additionally, a hysteresis region is present in the system such that different amplitudes are reached depending on whether the airspeed is increased or decreased. Multiple amplitudes are hence possible for the same airspeed. As reported by Barrero-Gil et al. [3], the inflection points of the C_{F_y} curve are responsible for this behavior. They studied the influence of the polynomial coefficients of C_{F_y}, and thus the location of the inflection points, on the hysteresis region for several C_{F_y} curves. For the case of the square section with two inflection points, it was shown that an increase in A, C and D leads to a decrease in the range of airspeeds where the hysteresis takes place while lower values of these coefficients increase the hysteresis region. The opposite is true for the B coefficient.

Finally, it has to be mentionned that the unstable part of the curve cannot be obtained experimentally nor through numerical integration since the system will not converge to that unstable solution. One way to obtain it would be to solve the equation of motion using approximate asymptotic methods such as the method of van der Pol, Hopf bifuractions or the method of multiple scales [11]. However, in this work, this would not be particularly useful since, as mentionned, it cannot be obtained experimentally. On top of that, when VIV ang galloping fully interact, the hysteresis region is no longer present, as will be shown later.

This theoretical S-curve will later be compared with the experimental results and will be used as a baseline for comparison with the case where VIV and galloping interact.

2.4.3 VIV-galloping interaction

For low-damping (very small ζ) and/or low-density structures (low n), the critical galloping velocity can become lower than the critical VIV velocity such that VIV and galloping interact. The resulting amplitudes can not be predicted by both theories separately.

Following the work of Corless and Parkinson [16], the two models described previously can be combined to model the interaction between the two phenomena. The simplest natural mathematical approach consists in adding linearly C_v and C_{F_y} on the right hand side of the equation of motion of the cylinder. It results in a second order nonlinear system of equations which can be written as

$$Y'' + Y = n(U_r^\omega)^2 \left(C_{F_{y,\zeta}} + C_v\right) \tag{2.43}$$

$$C_v'' + \nu^2 C_v = a(\nu)\left(C_v' - \frac{4}{3C_{Y_0}^2\nu^2}(C_v')^3\right) + D(\nu)Y' + B(\nu)Y'' \tag{2.44}$$

where the transverse force coefficient now includes the $2\zeta Y'$ term and whose expressions is

$$C_{F_{y,\zeta}} = A\left(1 - \frac{U_{r,g}^\omega}{U_r^\omega}\right)\frac{Y'}{U_r^\omega} - B\left(\frac{Y'}{U_r^\omega}\right)^3 + C\left(\frac{Y'}{U_r^\omega}\right)^5 - D\left(\frac{Y'}{U_r^\omega}\right)^7 \tag{2.45}$$

Therefore, $C_{F_{y,\zeta}}$ is modelled using the quasi-steady assumption while C_v is the unsteady force which is solution of the second equation of the system. A new inertial term has been added, $B(\nu)Y''$, to account for the effect of the cylinder acceleration on the wake. One can also note the dependence of the parameters a, D and B on the airspeed, whose functional forms will be taken as

$$a(\nu) = a_0\nu \qquad D(\nu) = \frac{d}{\nu} \qquad B(\nu) = \frac{b}{\nu^2} \tag{2.46}$$

with a_0, d and b scalar constants. These functional forms are chosen for several reasons. In particular, they should be simple, with as few constants as necessary. Regarding $a(\nu)$, it is the same as the one used originally by Hartlen and Currie. The two other forms are chosen by considering that for $\nu \to \infty$, the quasi-steady assumption implies that the wake oscillator terms become less important, as opposed to $C_{F_{y,2}}$ which becomes dominant. A detailed mathematical justification of these functional forms is described in a second work of Corless [11]. The free parameter's values of a_0, d, b and C_{Y_0} have to be determined using experiments.

Note that it is in fact the same model as the one used by Bouclin [8], where the new term including Y'' was absent. Additionally, an alternative model would be the one of Tamura and Shimada [23], which developed a similar model that also uses the wake-oscillator principle and summing the two excitation forces. The resulting system of equations contains only two free parameters which are the nondimensional width of the wake and a coefficient of proportionality of the lift coefficient to the wake inclination, which can be related to the Magnus effect for a rotating cylinder. Though the number of parameters to determine is smaller and they have a better physical meaning, they may be challenging to identify accurately hence the choice of the present model [6].

Parametric study

The free parameters of the model will now be varied in order to understand how they affect the behaviour of the response of the system. The parameters that will be modified are a_0, C_{Y_0}, d, b and, for the sake of completeness, one could also find it interesting to include the polynomial coefficients of C_{F_y}. When one parameter is varied, the others are kept equal to their "default" value and each parameter is varied by ± 20 %. The base values are the ones of Corless and Parkinson [16] (see Table 1) in order to respect the original values when the model was introduced. Notably, the value of C_{Y_0} is in quite good agreement with other subsequent studies on stationary square cylinders who determined $C_{Y_0}^{rms} \approx 1.1$ [24].

Parameter	a_0	C_{Y_0}	d	b	A	B	C	D
Value	0.13	1.40	0.855	-2.35	4.87	421	17000	194000

Table 1: Default values of the model parameters.

The influence of the parameters on the response amplitudes is depicted in Figure 2.9 and Figure 2.10. The mass and damping ratios are the same for all cases and correspond to the default experimental setup, discussed in the next section.

First, for all the wake oscillator parameters, it is generally observed that the asymptotic amplitudes are not affected, or barely, which is in agreement with the expected behaviour. More specifically, starting

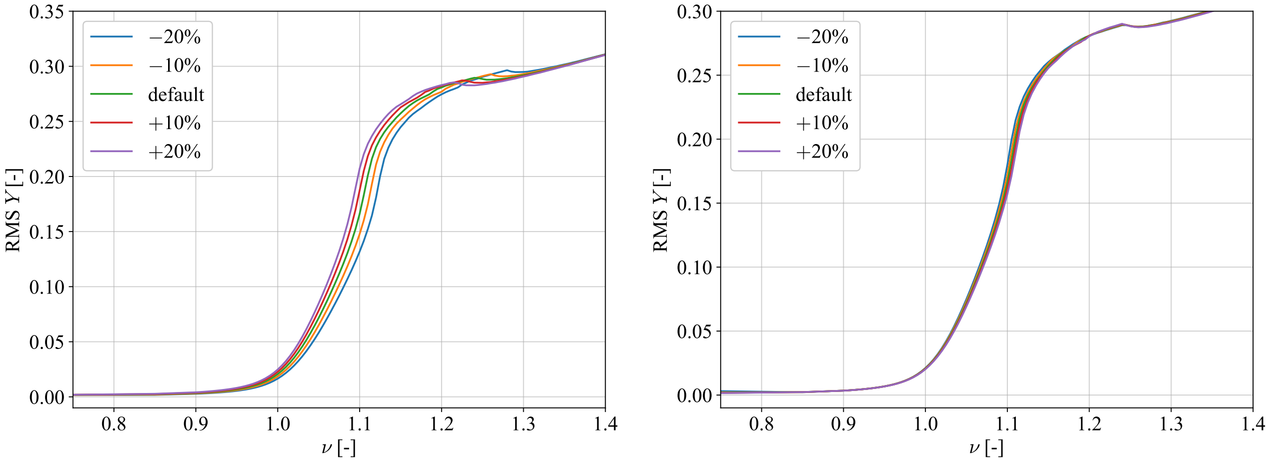

(a) C_{Y_0} (b) a_0

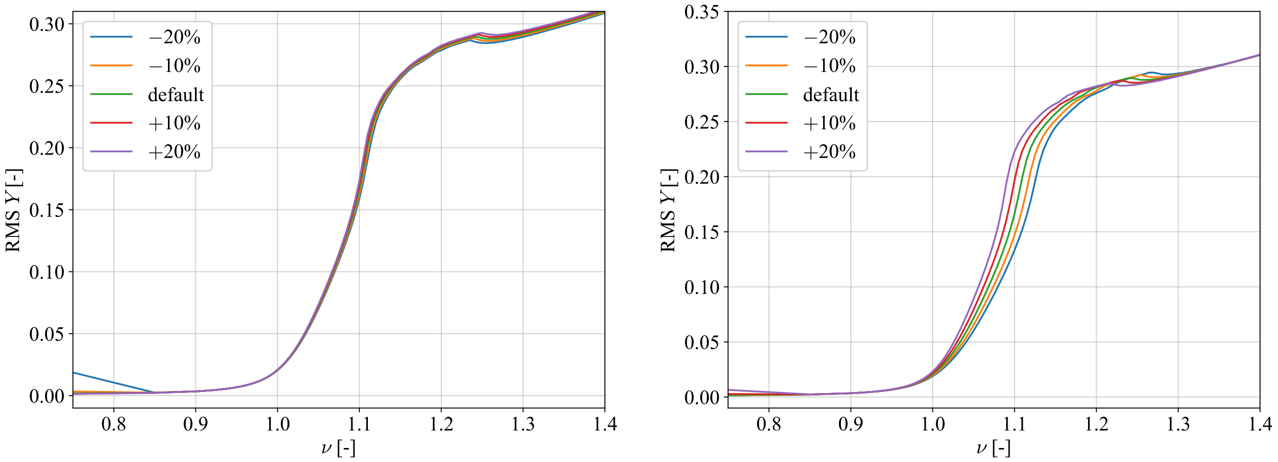

(c) d (d) b

Figure 2.9: Influence of the variation of the wake oscillator parameters on the amplitude response of the system. The values of $\zeta = 0.038$ % and $n = 5.5 \cdot 10^{-4}$ were used for all cases.

with C_{Y_0}, it can be seen that increasing this parameter increases the amplitude of vibration in the clutch shape part of the response, where the VIV contribution is the most important. Additionally, the kink of the curve is shifted to lower velocities and amplitudes as C_{Y_0} is increased, for the same reason. Then, for a_0, the model is a lot less sensitive to its value. Since it multiplies the linear and cubic damping terms in the wake oscillator equation, increasing a_0 makes damping more aggresive such that the system reaches faster LCOs, with no real influence on Y. Next, concerning the parameter d, its influence is mainly visible for $\nu > 1.1$. Increasing d shifts the kink of the curve to higher velocities and amplitudes since a larger value of d means a stronger coupling between the wake and the cylinder. One can notice the amplitude prediction for $\nu < 0.85$ if d is increased by 20 % which is not physical. Then, for b, which multiplies the inertial term, one observes that the system is quite sensitive to this parameter between $\nu = 1$ and 1.3. Decreasing b delays the growth of amplitude to higher velocities but increases the amplitude of the kink because the inertial coupling term between

Y and C_v is decreased and so is the forcing feedback from Y'' to C_v. The system needs thus more energy i.e. flow velocity to generate the kink and amplify the motion.

Regarding the polynomial coefficients of C_{F_y}, their influence is significant for $\nu > 1.2$, as expected in the galloping part of the response. The most important coefficient for galloping is A and increasing its value means that the system is more prone to galloping. As a result and as observed, higher amplitudes are reached, with a steeper asymptotic slope. The amplitudes below $\nu = 1$ for the two cases where A is increased should be discarded since it has no physical interpretation and sense. Then, for B, C and D, they affect considerably the asymptotic evolution of the amplitudes at large velocities but the physical meaning behind why an increase or decrease in their value affects in a certain manner the amplitude is limited. One can still notice an amplitude jump for the purple C curve and the blue D curve, where the system goes directly on the galloping branch without a kink.

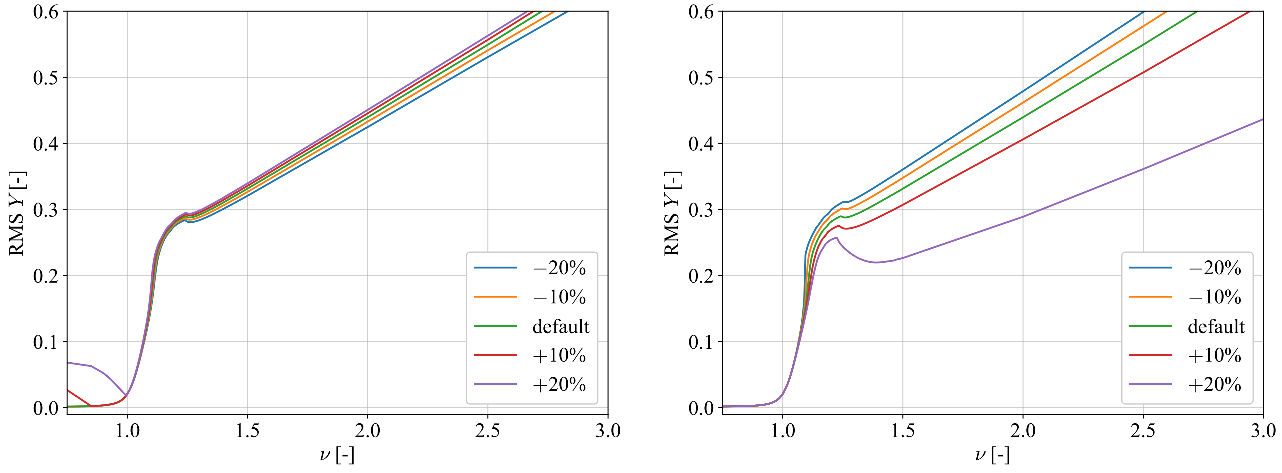

(a) A (b) B

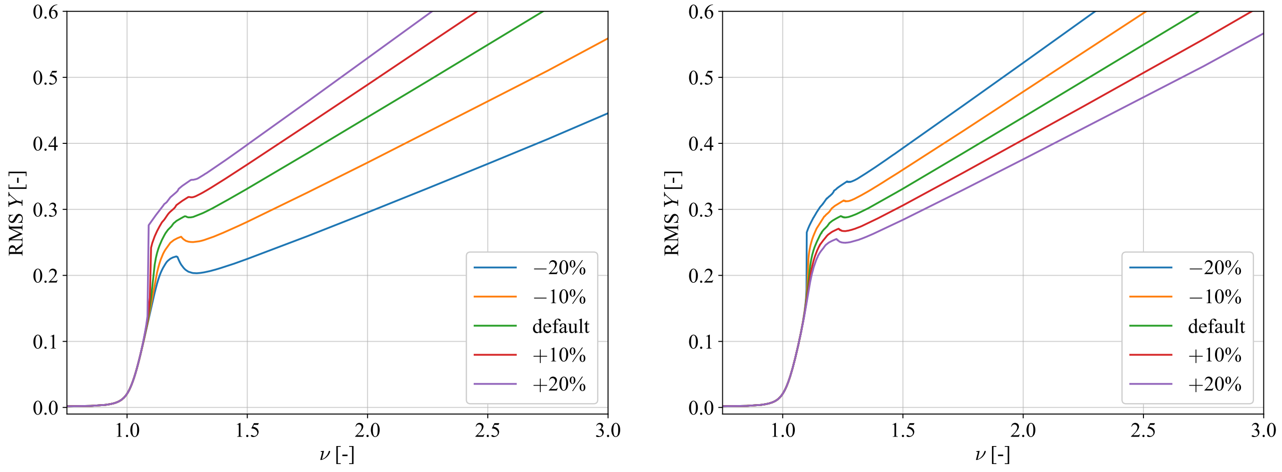

(c) C (d) D

Figure 2.10: Influence of the variation of the polynomial coefficients of C_{F_y} on the amplitude response of the system. The values of $\zeta = 0.038$ % and $n = 5.5 \cdot 10^{-4}$ were used for all cases.

Therefore, in order to calibrate the model, one has to keep in mind that for velocities near the critical VIV velocity, the wake oscillator parameters affect the most the response of the system, while beyond the kink of the curve, the system is dominated by the C_{F_y} excitation. The polynomial coefficients of the transverse force coefficient are hence the most important for the asymptotic behaviour of the curve.

Chapter 3

Aeroelastic testing

This chapter describes the experimental tests and a first part of the results that were conducted on a square cylinder in a wind tunnel. The experimental setup is first described with its main components. Then, the methods used for the determination of the frequency of the structure, damping ratio (with and without wind) and pressure on one slice of the cylinder are presented. Finally, a portion of the obtained data is presented.

3.1 Experimental setup

In this section, the experimental setup is described, beginning with an overview of the wind tunnel. It is followed by a detailed discussion of the overall setup and the key considerations involved. Finally, the various sensors employed in experiments are presented, along with a review of their calibration processes.

3.1.1 Wind tunnel

The experimental tests were conducted in the wind tunnel of the University of Liège. A schematic is presented in Figure 3.1. It is a closed loop subsonic tunnel and its modular design allows for reconfiguration into an open loop configuration. Moreover, it offers two different test sections and nozzles. Both sections include a rotating test table and air circulation is ensured by an electric fan with a power of 440 kW.

The first section is the aeronautic/automobile test section (TS1). This is the section that is used for the experimental tests of this work. Its general characteristics are reported in Table 2. The incoming flow of air is uniform and several sides and upper walls are made of glass to enable flow visualization using Particle Image Velocimetry (PIV), though it will not be used here.

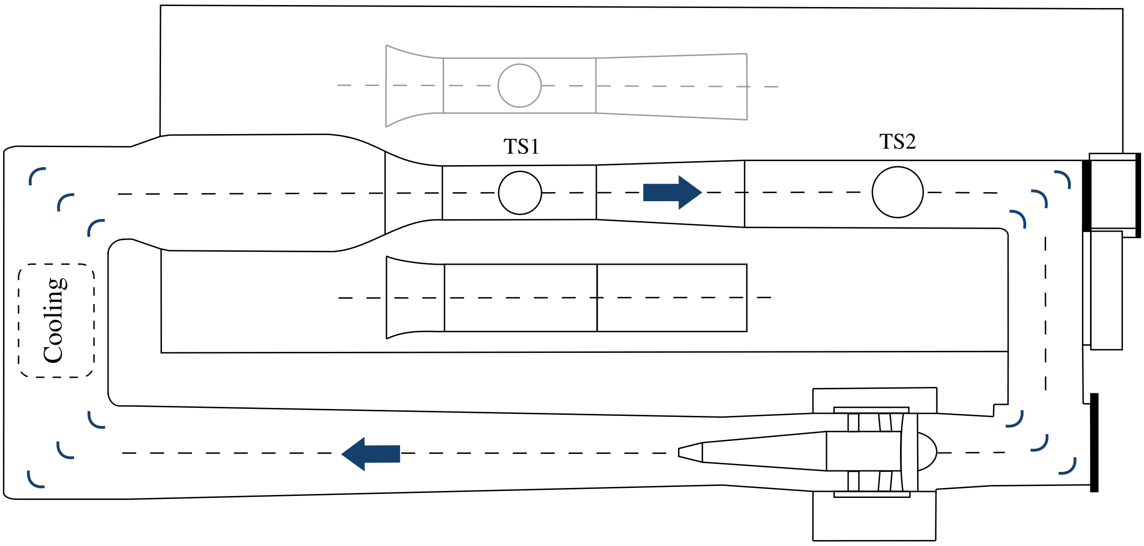

Figure 3.1: Schematic representation of the Uliège wind tunnel where the tests were performed, in TS1. Blue arrows indicate the wind circulating direction [31].

Characteristic	Value
Dimensions (Width x Height x Length)	2 m x 1.5 m x 5 m
Closed loop - speed range	2 - 60 m/s
Open loop - speed range	2 - 40 m/s
Test table	Diameter 1.5 m, rotation ± 90°
Thermal stability	$\approx$ 1°C
Speed non-uniformity	$<$ 0.5 %
Turbulence level	0.15 %

Table 2: Features of the test section 1 used for the experimental tests [31].

3.1.2 General setup

The model used is an aluminum hollow cylinder with a square section and sharp corners measuring 50 mm of side length and 600 mm of longitudinal length. The thickness of the cylinder sides is 2 mm. It is elastically mounted on four identical helical springs that enable the cylinder to vibrate along one transverse direction. An image of the setup is presented in Figure 3.2. It is placed with one side directly facing the flow hence at 0° angle of attack. This angle will not be changed throughout this work.

In this way, damping is low ($\zeta \ll 1$ %). No damping device is added, only rubber bands attached on each end of a spring and rubbing against it enables to increase damping. The wind-off damping ratio is determined before and after each aeroelastic test to check if it has changed during it.

Figure 3.2: Experimental setup in the wind tunnel, seen from upstream of the model.

The size of the model is limited by the blockage ratio which should not be greater than 5 %. Indeed, above this limit, the walls of the wind tunnel pertub the flow around the cylinder too much such that the results have to be interpreted with caution. Considering the frontal area of the square prism 50 mm × 600 mm, the blockage ratio is thus equal to 2%. Therefore, regarding this aspect, measurements are reliable and no blockage corrections should be applied to the measured data.

Additionally, a *Kimo*® hot-wire anemometer, fixed to the ground and visible on the left in Figure 3.2, is used to measure the free-stream velocity. It is important since the air velocity seen by the model differs, to a non-negligible extent, from the airspeed imposed by the fan due to the setup that alters the flow. Indeed, the experimental setup introduces blockage as opposed to no setup in the test section, which reduces the velocity of the air. The anemometer is located 0.65 m in front of and 0.6 m on the side of the cylinder to ensure it does not affect the air flow seen by the model substantially. The temperature of the air is also measured using the same device to determine the air density. The specifications of the anemometer are reported in Table 3 with the relevant accuracies and resolutions. The measurements by the anemometer will therefore be precise enough especially considering that the airspeed will be used to be associated with a LCO amplitude and to compute the pressure coefficients.

The cable visible in Figure 3.2 is used to power the pressure sensor, located inside the cylinder. The discussion on this sensor is more detailled in section 3.1.3.

Finally, in order to assess if 3D effects are important, experimental tests are conducted with end plates installed at each end of the model (Figure 3.3). They consist of two circular wooden panels with a diameter of 800 mm and a thickness of 5 mm. Moreover, they are fixed on the frame of the setup

	Measuring ranges	Accuracies	Resolutions
Air velocity [m/s]	from 0.15 to 3	± 3% of reading ± 0.03 [m/s]	0.01
	from 3.1 to 30	± 3% of reading ± 0.1 [m/s]	0.1
Temperature [°C]	from -20 to 80	± 0.3 % of reading ± 0.25 [°C]	0.1

Table 3: Specifications of the *Kimo*® anemometer placed upstream of the model [19].

such that there is a gap of about 5 mm between the cylinder and the end plates on both sides, enabling the cylinder to freely vibrate as with no end plates. The remainder of the setup remains the same as without end plates.

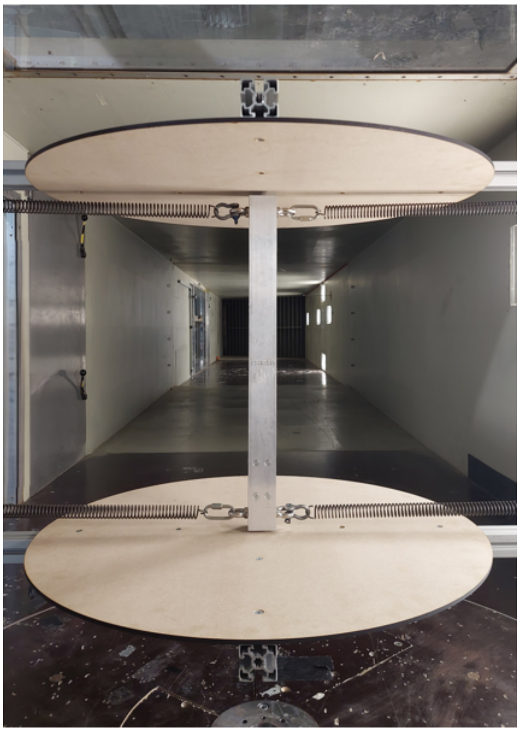

Figure 3.3: End plates installed on the experimental setup.

The end plates will thus ensure that the flow is two-dimensional and, since the cylinder is hollow, that no air can enter inside and produce undesirable effects. As a result, data collected with and without end plates will be compared to assess if these effects are significant. Note that no pressure measurements are performed with the end plates configuration since enabling the cable to go through the bottom plate would be cumbersome and certainly add unpleasant damping.

3.1.3 Instrumentation

Lasers

The amplitude of the cross-flow displacement (perpendicular to the wind direction) of the prism has to be measured for each airspeed. To this end, two *SICK*® *OD value P300W 200I0* [37] lasers attached to the frame were used, positioned at each end of the cylinder and individually measuring the distance separating them from the cylinder. Refer to Figure 3.4 for a close-up view of the lasers. They enable determining the amplitude of vibration while being contactless. Note that the rotational motion of the cylinder in the plane perpendicular to the flow can be computed from the difference in displacement measured by the two lasers. Only the translational motion is of interest, but the second laser was added to check for this potential rotational motion that could occur since it is not particularly constrained. The lasers' measuring range is 500 mm so the lasers are placed at 350 mm from the cylinder such that they are at an ideal distance and are able to measure large amplitudes of vibration while avoiding saturating them.

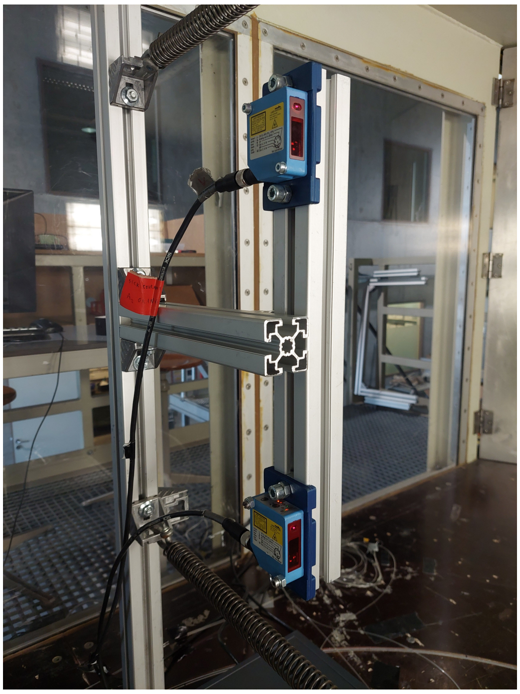

Figure 3.4: Lasers used to measure the cross-flow displacement of the cylinder.

The repeatability of the lasers is 0.1 mm and their linearity is ± 1.2 mm, ensuring precise measurements. Lastly, they are connected to an acquisition software, itself connected to a computer to treat the signals in the LabVIEW software [20].

Pressure sensor

In order to determine the forces acting on the cylinder during its motion, the pressure distribution is also measured at one slice at the mid-span of the cylinder. Each face has 8 pressure taps that consist in drilled holes and glued to each one of them lies a plastic tube that propagates the air pressure seen at the surface of the cylinder to the pressure sensor.

The pressure transducer used is the *nanoDAQ-32® Miniature Intelligent Pressure Scanner* which posesses up to 32 channels and greatly suits the needs of this work. Indeed, thanks to its small size (75 × 33 × 15 mm) it fits inside the cylinder. This way, all the pressure tubes don't have to come out of the cylinder, which would add damping and limit the VIV-galloping interaction. Indeed, it is preferable to have as low damping as possible and then add damping if desired. Only the power cable to power the sensor inside the cylinder is needed, which is of course better than all 32 tubes.

A snapshot of the sensor and its relevant data are reported in Figure 3.5 and Table 4 respectively. Several remarks can be made. First, adding the sensor inside will decrease the natural frequency of the system but only slightly due to the small mass increment. In fact, it only decreases by ≈ 3 % which will not pose any problem for the VIV phenomena. Secondly, the full scale corresponds to the maximum measurable pressure in PSI and the value used throughout the tests is 1 PSI = 6894.76 Pa which covers a large enough range of pressure for this work as verified afterwards during the tests.

Figure 3.5: Image of the pressure sensor [18].

Characteristic	Value
Available ranges (differential mode)	1, 2.5, 5, 15 and 45 PSI
Accuracy (range $\geq$ 1 PSI)	± 0.1% of full scale
Weight [g]	110
Resolution	16 bits

Table 4: Attributes of the *nanoDAQ-32®* pressure sensor [18].

Finally, an exploded view of the configuration holding the pressure sensor in place is depicted in Figure 3.6. It is boxed inside two 3D printed plastic casings that are bolted to the cylinder. Then, since the sensor is inside the cylinder, it is preferable to check that the motion of the cylinder does not influence (or at least it is negligible) the pressure measured by the sensor. To this end, a wind speed was set such that the vibration amplitude was 15 % of the side length of the cylinder. The pressure was recorded during motion but with the pressure taps covered in tape so that no pressure variations from the surface of the cylinder could be measured. As a result, it appeared that the sensor still measured ± 5 Pa, which is acceptable in comparison to the order of magnitude measured with no tape, which was measured to be between 50 and 100 Pa.

3.1.4 Calibrations

The stiffness of the springs and the output of the lasers measuring the displacement have to be determined. Indeed, the lasers output volts (V) that have to be converted to meters.

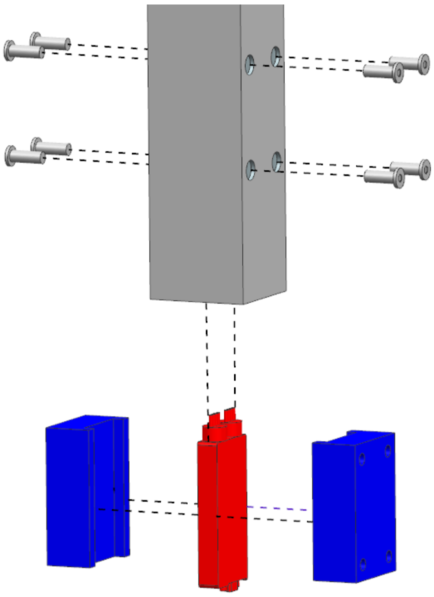

Figure 3.6: Exploded view of the pressure sensor (red) and the plastic casing (blue) inside the square cylinder.

To this end, simple known masses were added on top of the structure such that for each mass added, the mean output voltage was recorded and the displacement was manually measured. Plotting the laser output voltage in terms of the measured distance from the laser to the cylinder enables to determine which factor, having units of [V/m], has to divide the laser output to retrieve meters. This factor is equal to the slope of the line that fits the measurement points, as can be seen in Figure 3.7a.

The same principle is applied to determine the stiffness of the spring system by plotting the force applied by the springs following Hooke's law, which has to be equal to the weight of the added masses, in terms of the displacement. Similarly, the slope has units [N/m] and corresponds directly to the stiffness of the springs (see Figure 3.7b). As a result, the obtained values for the laser factor and the spring stiffness are, respectively, $K_{laser} = 10.07$ V/m and $k = 3357.01$ N/m.

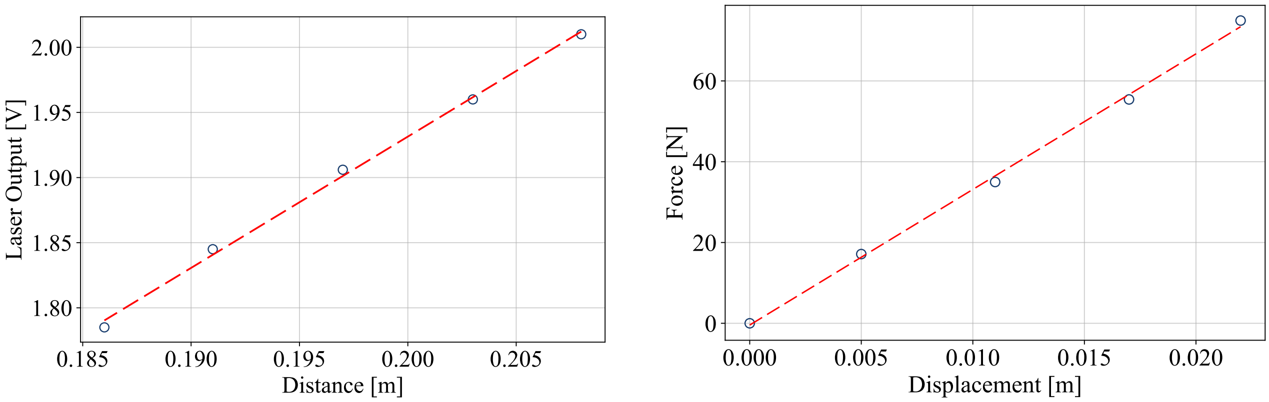

(a) Laser

(b) Springs

Figure 3.7: Calibration data used for the laser contant and the stiffness of the springs. ○ Measured data and — — linear fit.

3.2 Experimental methods

3.2.1 Damping determination

As damping is a crucial parameter in this work, a robust procedure and method(s) need to be used for its identification. Therefore, in order to determine the damping ratio ζ in wind-off conditions and when wind excites the structure, several methods will be used, allowing to have a better idea of the damping and mostly on the error made based on the sparsity of the results.

Frequency domain parameter estimation

The first method for estimating the damping ratio is the determination of the modal parameters through the theoretical expression of a one degree of freedom's frequency response function $H(\omega)$ namely

$$H(\omega) = \frac{A^*}{\omega_0^2 - \omega^2 + 2j\zeta\omega_0\omega} \tag{3.1}$$

where A^* is the residue, ω is the forcing circular frequency and $j = \sqrt{-1}$. Provided initial guesses for ω_0 and ζ, a nonlinear optimization can be performed to find the best values of these parameters that fit best the Fourier Transform (FT) of experimental data. It is achieved through the minimization of the error between the theoretical and experimental FT. Since it is a single degree of freedom method, it assumes that the modes are well separated, which is the case here.

Amplitude dependency of damping

So far, damping was considered linear hence the same for every amplitude of vibration. However, it is interesting to compute the evolution of the damping ratio in terms of the amplitude to see if the system exhibits nonlinear behaviour. To this end, similarly to the log-decrement method, the peaks of the signal are first located. Then, from successive peaks y_1 and y_2, with $t_1 < t_2$, the logarithm decrement δ is computed as

$$\delta = \ln\left(\frac{y_1}{y_2}\right) \tag{3.2}$$

and the damping ratio is retrieved through the relation

$$\delta = \frac{2\pi\zeta}{\sqrt{1-\zeta^2}} \quad \longrightarrow \quad \delta \approx 2\pi\zeta \tag{3.3}$$

since $\zeta \ll 1$ in this work. By locating the peaks and computing ζ, one can thus associate an amplitude of motion to each damping ratio and get the evolution of ζ in terms of y. In practice, for experimental data, there is a lot of noise at low amplitude so instead of using each peak successively, it is preferable to use one every p peak. Hence, for example for the first peak, the logarithm decrement δ is determined using

$$\delta = \frac{1}{p} \ln \left(\frac{y_1}{y_{p+1}} \right) \tag{3.4}$$

The value of p is chosen to remove as much noise as possible while still keeping enough data points for an accurate damping determination. This is the most robust method since even if the system shows nonlinear characteristics, the damping ratio can be computed as the mean damping ratio below a certain amplitude, to only retain the zero-amplitude damping in wind-off free decays.

As a summary, the methods to determine the damping ratio from the frequency domain and by considering the dependence of damping on amplitude described above are shown in Figure 3.8 as an example. It can be deducted that the estimation of damping using the FT works best when the response is close to linear because otherwise, it computes approximately the mean damping ratio for all amplitudes as shown.

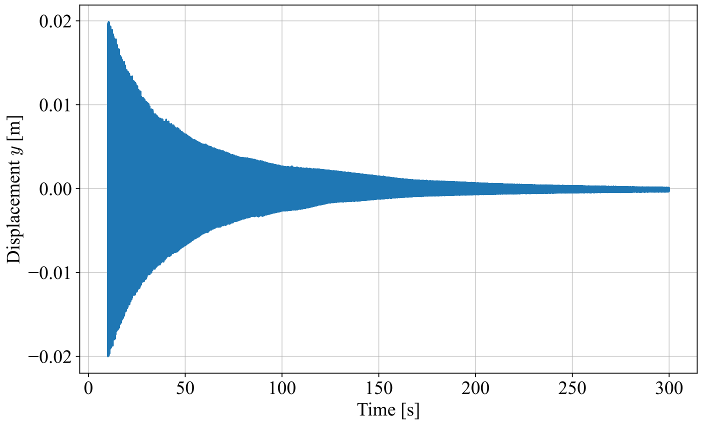

(a) Wind-off free decay signal.

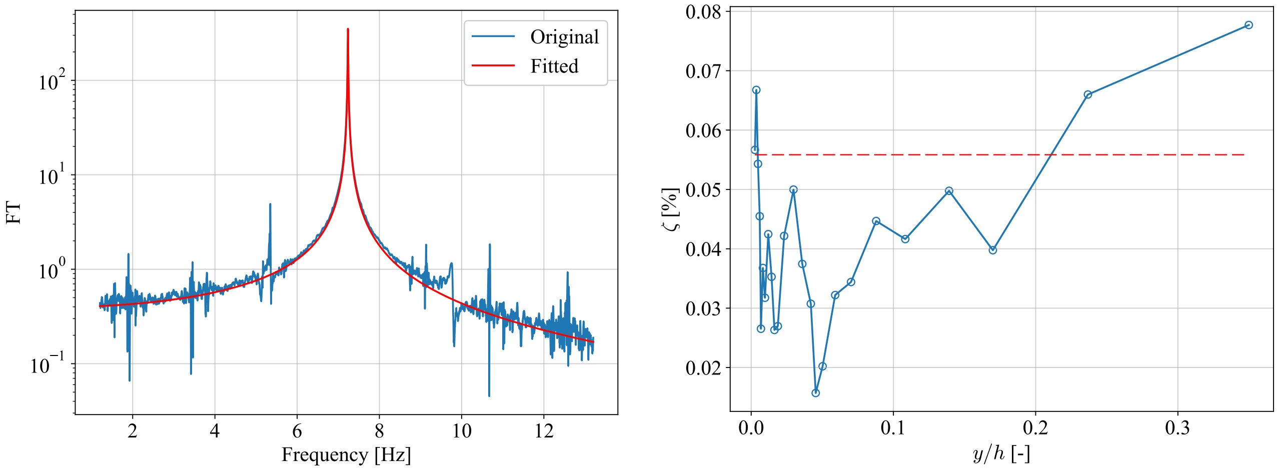

(b) Frequency domain estimation - $\zeta = 0.055$ %.

(c) Mean ζ below $y/h < 0.1$ - $\zeta = 0.038$ %.

Figure 3.8: Example of damping determination for a free decay signal. The red dashed line on the bottom right is the damping ratio determined with the FT approach for comparison.

3.2.2 Pressure measurements

The acquisition of the pressure at one section of the cylinder enables determining the forces acting on it during its motion. The determination of these force coefficients is presented here.

Firstly, for each pressure tap, the pressure values $p(t)$ are adimensionnalized through the pressure coefficient, defined as

$$C_p(t) = \frac{p(t) - p_\infty}{\frac{1}{2}\rho U_\infty^2} \tag{3.5}$$

where p_∞ is the static reference pressure and $\frac{1}{2}\rho U_\infty^2$ is the dynamic pressure. The time-mean pressure coefficient will be noted $\bar{C}_p$. From the distribution of this pressure coefficient around the square section, the 2D force coefficients acting in the direction of the flow and perpendicularly can be computed. Indeed, the differences in pressure coefficients between the two side faces, denoted $\Delta C_{p,y}^i$, and between the front and back faces, denoted $\Delta C_{p,x}^i$, are first computed for each pressure taps opposite each other. Then, the transverse and streamwise force coefficients are computed respectively as

$$C_{F_y} = \sum_{i=1}^{8} \frac{1}{h} \Delta C_{p,y}^i \Delta s \qquad\qquad C_{F_x} = \sum_{i=1}^{8} \frac{1}{h} \Delta C_{p,x}^i \Delta s \tag{3.6}$$

where the surface element for each pressure tap is $\Delta s = \frac{h}{8}$ since there are eight of them per face. Looking back at Figure 2.5, the lift and drag coefficients are determined by taking into account the cylinder's motion and the relative velocity from

$$C_L = -C_{F_y} \cos\alpha - C_{F_x} \sin\alpha \tag{3.7}$$

$$C_D = C_{F_x} \cos\alpha - C_{F_y} \sin\alpha \tag{3.8}$$

These coefficients show how the air affects the cylinder and will be used to study the flow-structure interaction. The relative angle of attack α is determined from the displacement measurement y, which is differentiated with respect to time to get $\dot{y}$ and then divided by U_∞.

3.3 Wind tunnel tests

Now that a robust and reliable experimental setup is established, experimental tests can be conducted. As a starting point, the results that will be presented here are the dependence of the amplitude of vibration of the square cylinder on the airspeed and the pressure measurements on one slice at the mid-span of the cylinder. Numerical results are not discussed and are reserved for chapter 4.

3.3.1 Amplitude results

This section presents and discusses the experimental results obtained for the amplitudes of vibration of the square cylinder as the wind speed increases. The influence of damping is first presented, with several configuration that are compared. Then, a comparison with and without end plates is carried on to check if the two-dimensional flow enforced with end plates significantly affects the results.

Damping influence

In order to determine the structural damping ratio for a particular configuration, the methods described before are used on free decays in wind-off. To check for nonlinearity, the influence of the amplitude on damping is assessed and the damping ratio retained with that method is the average damping below a reduced amplitude of $Y < 0.1$ or higher if data at these low amplitudes were missing. The natural frequency of the structure is determined simply as the frequency corresponding to the peak of the Fourier Transform of the free decay. The damping ratio ζ, natural frequency f_0, mass ratio n and Scruton number Sc are hence determined for each configuration and reported in Table 5. The configurations here include, in order, one with the pressure sensor cable (1), one without it (2), which reduces damping, one without the cable and no sensor inside but with thin rubber bands to add a small amount of damping (3), and one without the cable and no sensor inside (4).

	Configurations			
Parameters	(1)	(2)	(3)	(4)
ζ [%]	0.038	0.026	0.015	0.01
f_0 [Hz]	7.24	7.26	7.51	7.44
n [-]	$5.5 \cdot 10^{-4}$	$5.5 \cdot 10^{-4}$	$6.0 \cdot 10^{-4}$	$6.1 \cdot 10^{-4}$
Sc [-]	4.3	2.9	1.6	1.0

Table 5: Damping ratio ζ, natural frequency f_0, mass ratio n and Scruton number Sc of each configuration.

The amplitude-velocity dependence for various structural dampings is depicted in Figure 3.9. The root mean square (RMS) of the reduced amplitude is used to attenuate the effects of noise. The tests were stopped when the oscillating cylinder started shaking the frame of the setup too much and/or the cylinder started going rearwards due to drag, indicating the limits of the setup.

First, it appears that all configurations start to vibrate at the same velocity, namely the critical VIV velocity at $U^r_{VIV} = 1/St \approx 7.7$, independently of structural damping. Therefore, the oscillations are initiated by vortex-induced vibrations i.e. the frequency matching between the vortices shed in the wake of the cylinder and the structural natural frequency. However, unlike VIV, the amplitude keeps growing with wind speed and never decreases. The stability of the structure is lost and never recovered. It is also clear that as structural damping decreases, higher amplitudes are reached, which is in accordance with the galloping theory. Note that this observed behaviour can not be only VIV due to the high amplitudes reached and the lock-in range that would be excessively large.

The cricital galloping velocity for each configuration is also shown. As can be seen, there are all lower than U^r_{VIV}, suggesting that a strong interaction between VIV and galloping occurs. These

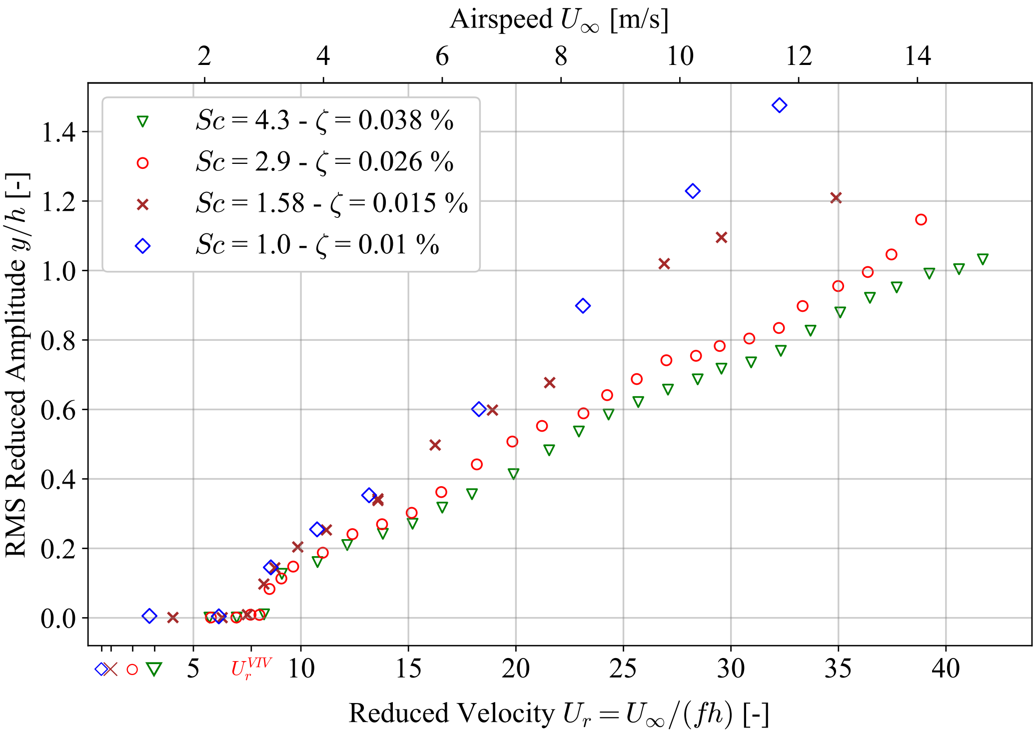

Figure 3.9: Amplitudes of vibration in terms of wind speed for several structural dampings. The colored markers on the horizontal axis correspond to the critical galloping velocities of each configuration. Re ranges from $3 \cdot 10^3$ to $5 \cdot 10^4$.

critical velocities are computed using the quasi-steady theory but since damping is so low, $U_{r,g}$ is also small such that the quasi-steady theory is no longer valid. Indeed, galloping does not start at the predicted velocity. Moreover, due to the large interaction between VIV and galloping, only one branch of galloping is present and the lower amplitude branch is not observed. The system appears to start with VIV then jump directly on the upper branch of galloping. As reported by Mannini et al. [4], this phenomenon is called the quenching effect and occurs when the critical galloping velocity is lower than the critical VIV velocity. Vortex shedding is able to stabilize the cylinder up to U_r^{VIV} hence the name of quenching which means “suppressing” in this context. Multiple authors have shown that the phase angle between the force and the motion is negative below U_r^{VIV} indicating that aerodynamic damping introduced into the system is positive, as opposed to the negative damping predicted by the quasi-steady theory.

End plates influence

By altering the flow at the cylinder ends, end plates can reduce three-dimensional effects. It can lead to noticeable changes in the amplitude of flow-induced vibrations. As mentionned when presenting the experimental setup, no pressure measurements are made in the presence of end plates. In this section, the amplitude results with and without end plates are compared in order to better understand their impact on the dynamic response of the structure.

To conduct this comparison, two configurations with approximately the same Scruton number are considered to only study the influence of the end plates. The amplitude-velocity plot for both configurations is presented in Figure 3.10. It can be seen that the presence of end plates does not influence much the amplitude of vibration of the cylinder, for all the airspeeds considered. It means that the flow without end plates is already two-dimensional to a great extent. The importance of 3D effects can be assessed by computing the aspect ratio which, for a square cylinder, is simply the ratio between its longitudinal length and side length i.e. l/h. It is thus equal to 12, which is rather large, indicating that the cylinder is in fact slender and the tip effects don't affect a large portion of the cylinder.

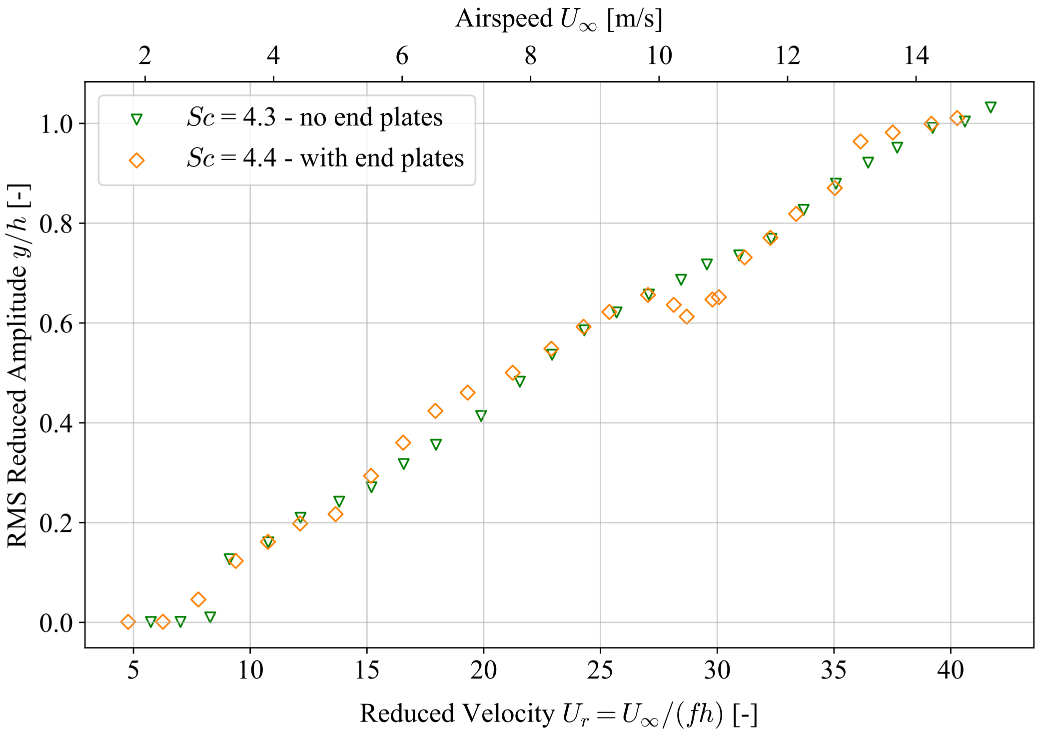

Figure 3.10: Comparison of the amplitudes between configuration (2) with and without end plates.

Moreover, bluff bodies, especially symmetric ones such as a square cylinder, do not produce a large difference of pressure since their geometry does not create considerable lift. These effects at the tips are hence small as opposed to wings for instance, which are designed to produce a maximum amount of lift and for which tip effects can be significant.

Therefore, the results obtained without end plates are reliable and comparable to results that would be obtained in two-dimensional flow conditions. The rest of this work will thus use the configuration without end plates, enabling to measure the pressure distribution at the mid-span of the cylinder.

3.3.2 Pressure results

The pressure measurements will now be presented. Determining the pressure distribution around the cylinder enables to compute the forces acting on it namely the lift and drag. First, the mean pressure distribution at the mid-span of the cylinder is computed for an amplitude ratio of $y/h = 0.1$. The result is depicted in Figure 3.11 with two experimental references. The pressure distribution is thus fairly close to the other results. The pressure coefficient reaches 1 at the stagnation point in the middle of the front face since the velocity is zero there. Also, $\bar{C}_p$ is negative for the rear and side faces due to flow separation which creates vortices, and increases the velocity locally. Finally, it is more or less constant at the rear face due to the recirculating region and, for the side faces, decreases progressively downstream.

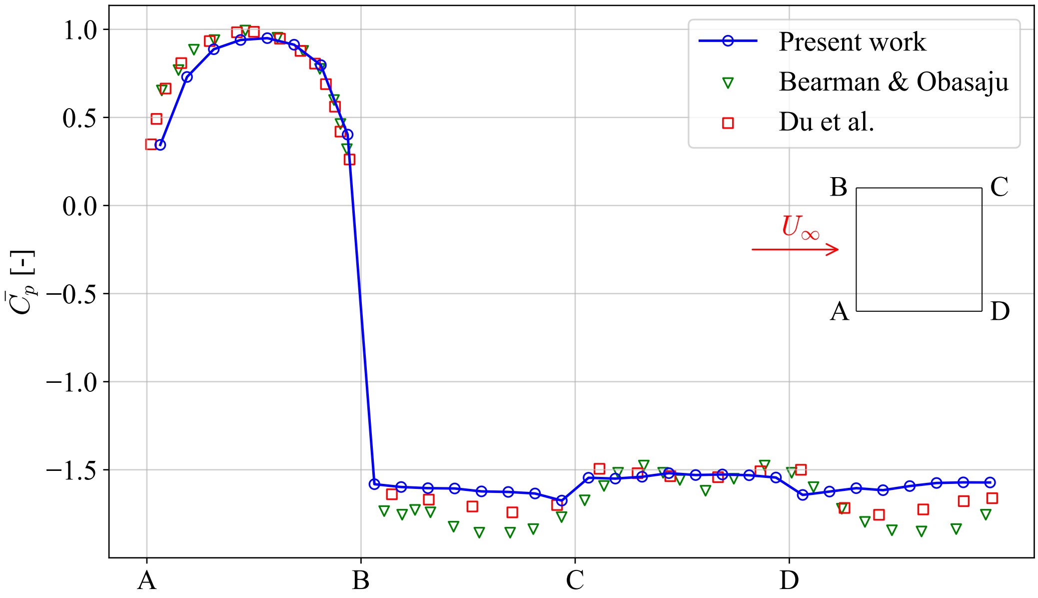

Figure 3.11: Mean pressure coefficient distribution at the mid-span of the square cylinder for configuration (1) and at $y/h \approx 0.1$, along with experimental references [12] [13].

It is useful to look at the aerodynamic coefficients in terms of the wind speed in order to better understand the phenomenon at play.

Consider Figure 3.12 where C_L^{rms} is plotted in terms of the RMS of the reduced amplitude. The results of the work of Tamimi et al. [26] performed in a water channel for similar Re varying between $3 \cdot 10^3$ and $4 \cdot 10^4$ are also depicted for comparison. It can be seen that both experimental results are reasonably close and follow the same trend, even if a higher magnitude is obtained globally. The RMS of lift coefficient is first large for low amplitudes (RMS of $y/h \leq 0.3$), which corresponds to VIV and results from the fact that, in lock-in, the cylinder's motion locks the vortex shedding frequency to its own oscillation frequency. This synchronization leads to an increase in the amplitude of the fluctuating lift force. For higher amplitudes, C_L^{rms} drops and plateaus at some point, which corresponds to the galloping regime. This behavior is primarily due to the quasi-steady aerodynamic forces that dominate in galloping at large amplitudes, as opoosed to VIV where the excitation comes from a periodic fluctuating force. Indeed, at large amplitudes, the coherent vortex shedding that is characteristic of VIV can be disturbed. The wake can undergo transitions to different vortex shedding modes, effectively reducing the lift coefficient.

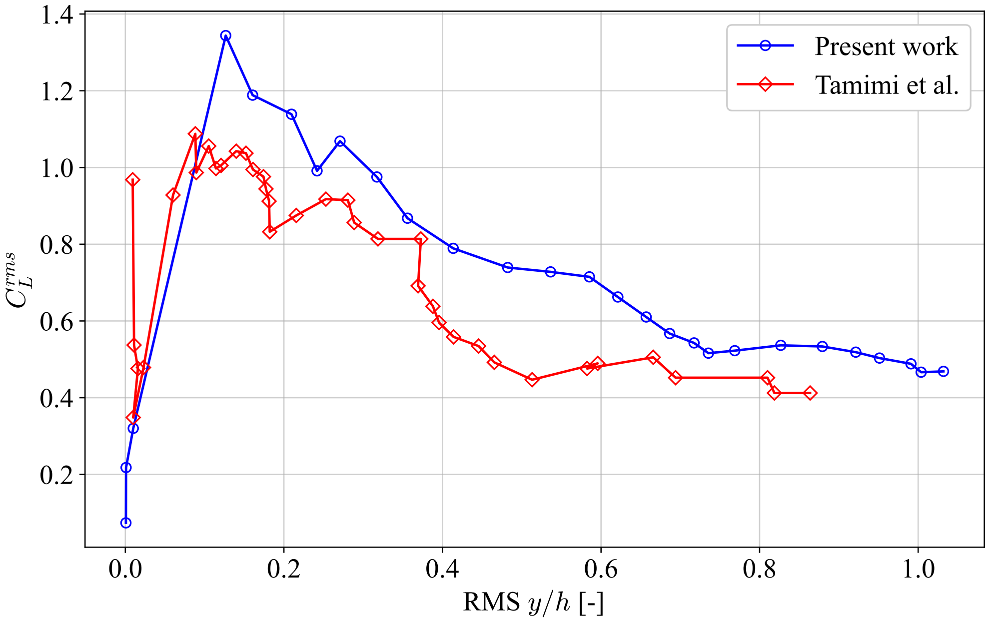

Figure 3.12: Evolution of the RMS of the lift coefficient as a function of the transverse amplitude of motion for configuration (1) and from Tamimi et al. [26].

This change in C_L^{rms} with increasing amplitude shows the shift from the VIV regime, caused by resonance, to the galloping regime. During this transition, changes in the wake pattern likely have a strong influence on the lift fluctuations.

Now, the lift and drag coefficients will be studied in the frequency domain. To this end, the evolution of their Fourier Transform (FT) in terms of the wind speed is computed for configuration (1). The FT is calculated for each airspeed and normalized, as depicted in Figure 3.13. The frequency f contained in C_L and C_D is divided by the natural frequency of the system $f_0 = 7.24$ Hz. The Strouhal law is also added to have a comparison with the vortex shedding frequency.

First, for the lift coefficient, when the reduced velocity is below 6, the cylinder does not have any transverse oscillations such that the frequency content of C_L is mainly noise. However, one can notice the frequency associated with the vortex shedding frequency of the Strouhal law that is present. This is expected, as even in the absence of transverse motion, the wake imposes periodic pressure fluctuations.

Then, as the wind speed is increased, the natural frequency f_0 is always the most important component in the lift coefficient spectrum, since the whole cylinder is always vibrating at the that same resonant frequency. One can also clearly see the presence of harmonics at even and odd multiples of f_0. These harmonics become particularly pronounced when they coincide with frequencies predicted by the Strouhal law, underlining a nonlinear interaction between the fluid forcing and the structure. This interaction amplifies frequency components that are reinforced by vortex shedding.

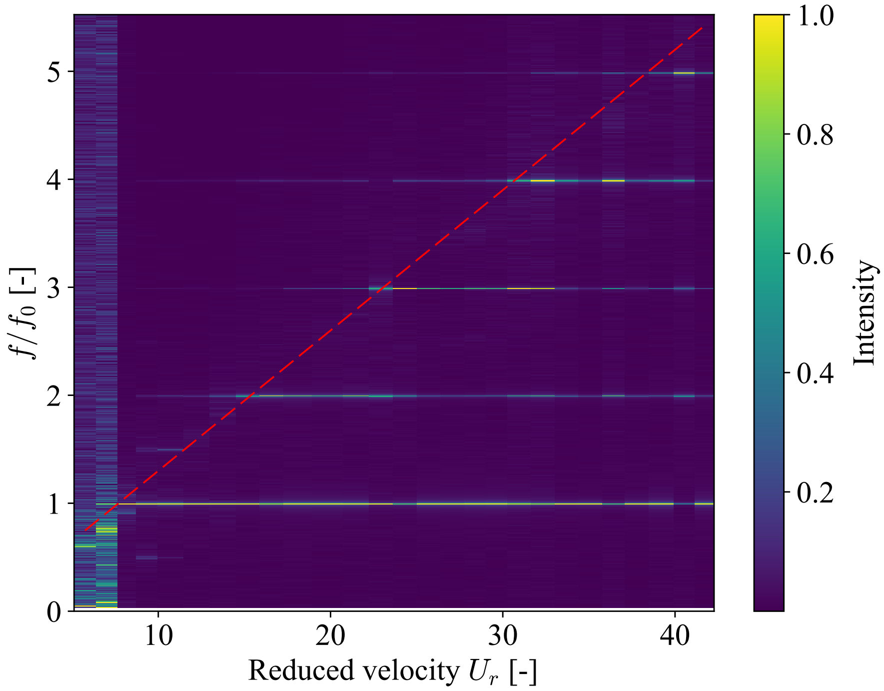

(a) Lift coefficient C_L

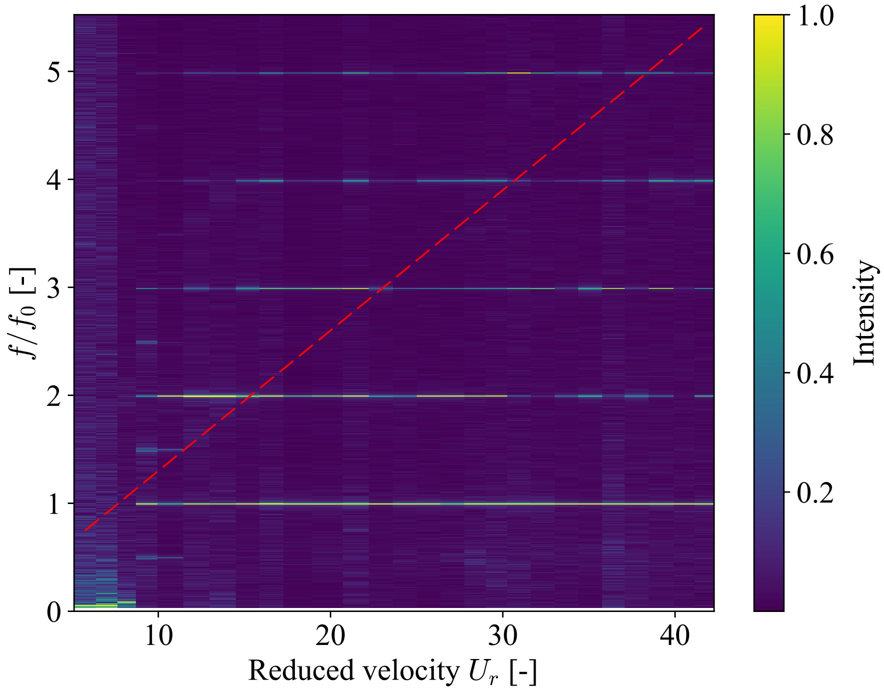

(b) Drag coefficient C_D

Figure 3.13: Evolution of the Fourier Transform of the aerodynamic coefficients in terms of the wind speed. The red dashed line – – – is the Strouhal law.

Concerning the drag coefficient, the same observations are made with harmonics that are present for lower airspeeds. The frequency content is also richer for lower reduced velocities. In any case, the presence of twice the vortex shedding frequency in the drag spectrum is expected since vortices are shed alternately from one side to the other, making the drag vary at twice that frequency.

Overall, both figures reveal frequency spectra rich in harmonics as the flow velocity increases. The alignment of harmonic peaks with the Strouhal frequency emphasizes the complex coupling between wake dynamics and structural motion.

Chapter 4

Experimental and numerical comparison

This chapter details the comparison between the obtained experimental and numerical data regarding several aspects. The comparison is first led by examining the amplitude of motion in the amplitude-velocity plane. Then, the system is analysed as it converges to LCOs from rest by looking at the evolution of the damping ratio and the frequency content of the signals. Finally, thanks to the pressure measurement performed, the experimental excitation force is compared to the numerical model results.

4.1 Amplitude prediction

First, the model predictions concerning the transverse amplitude of the cylinder are addressed. To this end, the coupled equations of motion presented in section 2.4.3 are integrated numerically using the explicit Runge-Kutta 45 method. For the initial airspeed considered, the initial conditions are set to $Y(0) = 0.01$, $Y'(0) = 0$, $C_v(0) = 0$ and $C'_v(0) = 0$. The system is integrated in time until LCOs are reached. As the wind speed is increased, the initial conditions for the next airspeed are taken to be the final state of the previous wind speed, mirroring the wind tunnel tests for an appropriate comparison. The results are also compared with the galloping-only response to assess how its interaction with VIV affects it.

Additionally, in order to account for the uncertainty on the parameters of the model, instead of fixing values, the comparison will be carried by considering a range of values for the model parameters. Therefore, the model will predict a region of amplitudes instead of a single curve. The region is limited by the outermost curves in the parametric study performed above. This way, all the parameter variations are included in the prediction region. The parameters are still varied by $\pm$ 20 %.

The comparison is made for configuration (1) and (2). The model is run using the corresponding mass and damping ratios. The galloping-only model is also included as reference and the result is depicted in Figure 4.1. In both cases, the general trend is quite well modelled. It can be seen that for reduced velocities below 17, the model overpredicts the amplitude, with a rapid rise that is not as sharp as experimentally. Then, there is a rather good agreement for higher U_r. The experimental data fits inside the prediction region of the model and gets closer to the model with default parameters, especially for the lower damping configuration. The slope of the asymptotic behavior is also well predicted in both cases. The source of discrepancies might come from the fact that, at low U_r, VIV effects dominate, which involve complex vortex shedding dynamics that are unsteady and poorly captured by a simple model, especially due to the quenching effect of galloping by VIV. The simple linear addition of the two excitations might also play role. Then, at high U_r, galloping dominates, which is generally well modelled by the quasi-steady theory.

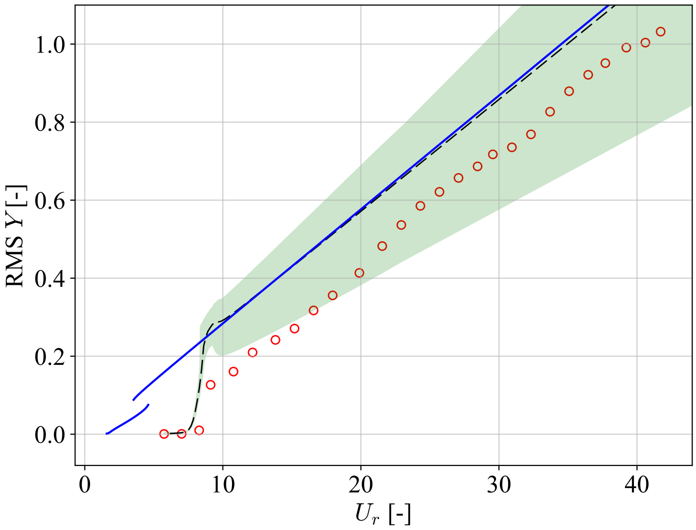

(a) ζ = 0.038 %

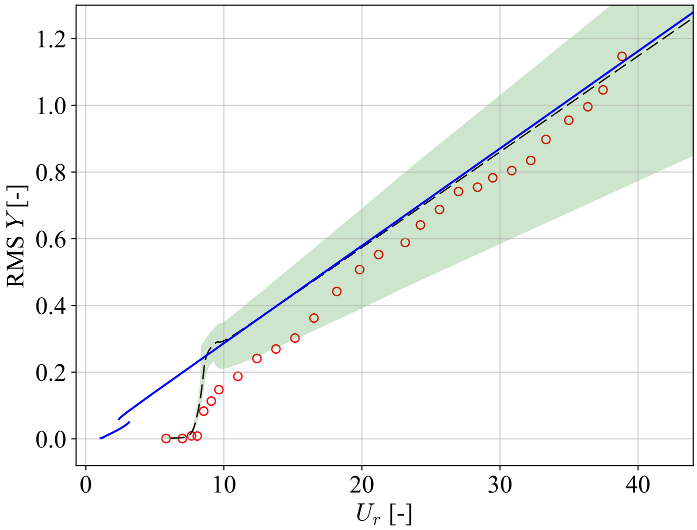

(b) ζ = 0.026 %

Figure 4.1: Comparison between the model and experimental measurements for $n = 5.5 \cdot 10^{-4}$ and for two different damping values. ○ Experimental data, – – Model with default parameters, 🟩 Prediction zone of the model with parameters varied by ± 20 % and — Galloping-only model.

It can also be seen that the galloping-only model ends up joining the combined model for $U_r \geq 10$

such that both models predict very close amplitudes. This comes from the fact that the coupling terms in the combined model are inversely proportional to the wind speed, making them tend to zero as it is increased. However, the same slope is not retrieved though they remain close. The effects of VIV are still present in the model even if they are minimal and it still influences the asymptotic behaviour.

Therefore, where VIV is the most dominant and where the interaction is the most pronounced, the model performs the worst. Nonetheless, for large amplitudes, the model is quite accurate and is to some extent reliable on the prediction of amplitudes.

4.2 Transient analysis

Another interesting aspect that has not been addressed so far concerns the transient amplitudes that the system exhibits when converging to LCOs. It is of particular interest to study how the oscillations develop depending on the airspeed. To this end, experimental measurements of the amplitudes building up from rest were performed for several wind speeds. The cylinder motion was first stopped down to zero amplitude then nudged out of its equilibrium position. The measurements ended when LCOs were reached. This section presents these experimental results and a comparison with the numerical model combining VIV and galloping.

Two examples of such transient signals are depicted in Figure 4.2. It can be seen that the amplitudes start to increase slowly but are followed by a continuously faster increasing amplitude regime. It also seems sharper for the higher velocity case. Then, as the system approaches the limit cycle, the amplitude increase slows down. There are in fact two inflection points in the envelope. Additional insight can be gained by looking at the evolution of the damping ratio over time or equivalently in terms of the amplitude.

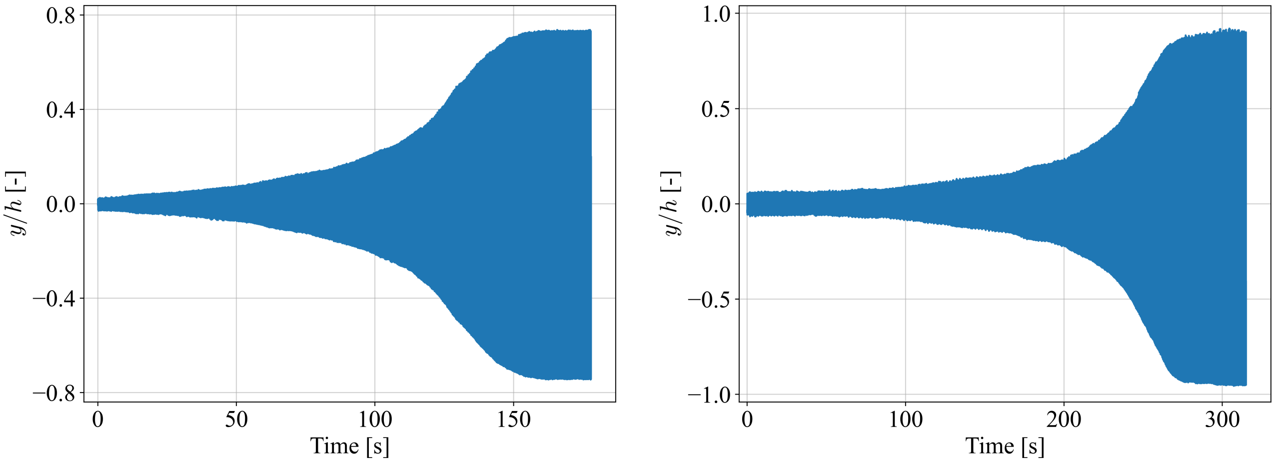

(a) $U_r = 21.8$

(b) $U_r = 27.6$

Figure 4.2: Examples of two transient signals for configuration (2) at different wind speeds, where the system reaches LCOs from rest.

To this end, the method described previously that uses the logarithm-decrement to determine ζ in terms of the reduced amplitude Y is used. This procedure is done on both experimental and numerical data in order to compare both. The configuration with no pressure measurements is considered since it enables to reach higher amplitudes. The experimental results are presented on the left in Figure 4.3. As the amplitude grows, damping is always negative. At low amplitudes, the system evolves slowly such that damping is close to zero. It can be seen that the system stars at zero amplitude with a higher damping for higher airspeed so the amplitude grows slower. Then, as the amplitude increases, the signal grows faster, and damping becomes more and more negative until reaching a minimum, where the signal grows the fastest and seems to jump to a higher energy-state. This minimal point is shifted to higher amplitudes for higher wind speeds. Finally, damping increases close to linearly until zero where LCOs are reached. As a result, the system takes a longer time to reach LCOs as the airspeed is increased since damping is less negative and also simply because it reaches higher amplitudes.

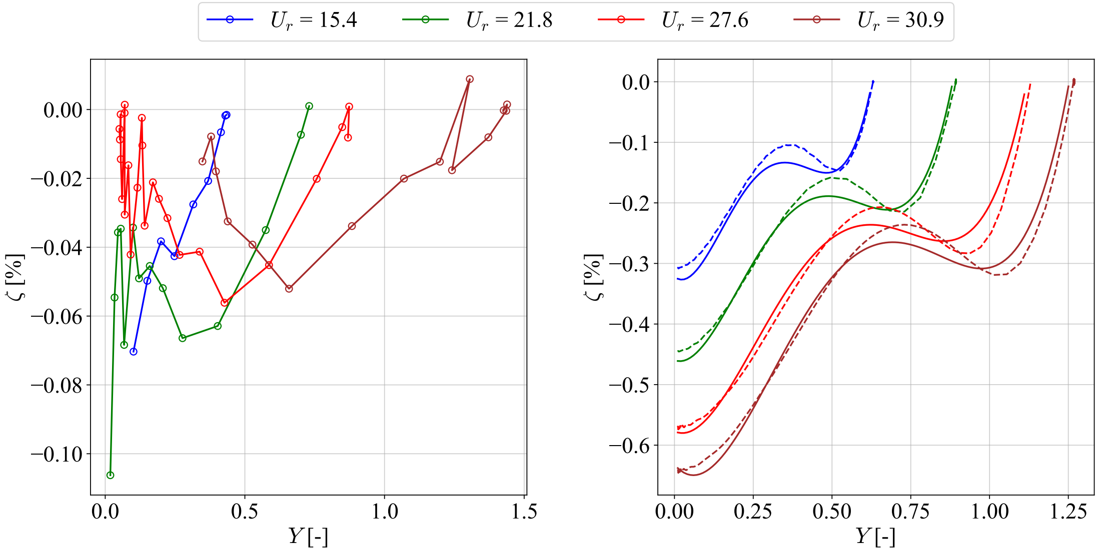

Figure 4.3: Comparison between experimental (left) and numerical (right) variation of the damping ratio in terms of amplitude for transient signals. The color code for both plots is the same. The solid line corresponds to the combined model while the dashed line is the galloping-only model.

The prediction of the numerical model combining VIV and galloping is also depicted on the right in Figure 4.3. The same trend is observed, with the minimum point of damping shifting to higher amplitudes with airspeed such that the convergence to LCOs is slower. However, the model predicts a lower damping ratio for higher wind speeds as opposed to the experimental measurements. Moreover, the damping ratio of the numerical model is greatly overestimated by almost a factor of 10. It is not clear why the model presents such low damping. Another difference is that at low amplitudes, damping decreases with airspeed as opposed to the experimental data. The general trend is correct but the damping values cannot be trusted. One cause of this large difference in damping ratio values might come from the nonlinear cubic damping term in the equation of the wake oscillator that is not increasing enough the damping of the system. Note that the curves of the models use the default parameters and that a variation of ± 20 %, shown in Figure 4.4, does not improve the difference in order of magnitude and tends to have a sharp drop to lower damping ratios.

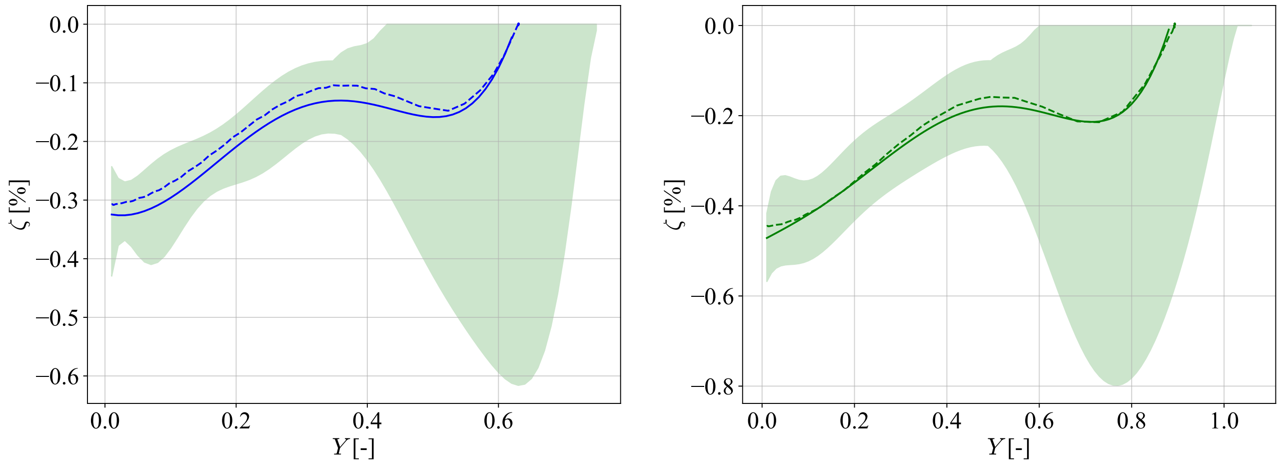

(a) U_r = 15.4 (b) U_r = 21.8

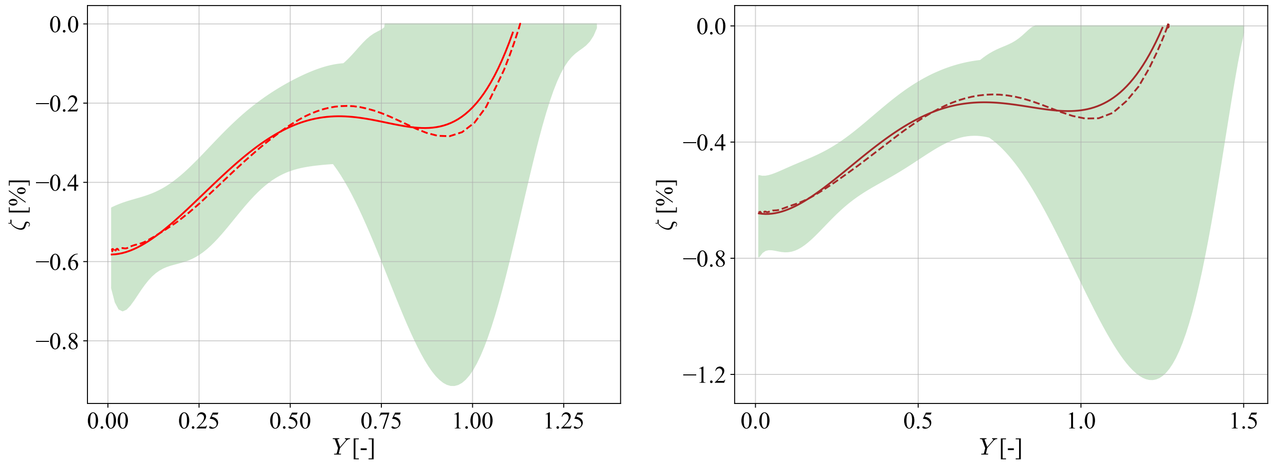

(c) U_r = 27.6 (d) U_r = 30.9

Figure 4.4: Variation of the zones of prediction of the model (🟩) for the transient evolution of the damping ratio as the model parameters are varied by ± 20 %. The solid line corresponds to the combined model while the dashed line is the galloping-only model.

Lastly, it is worth adding that, as also observed by Mannini et al. [5] for a rectangular cylinder, above a certain reduced velocity, a sufficiently high initial condition has to be given to the system in order for it to reach LCOs. Consider Figure 4.5 where the system is let evolving after two different initial amplitudes and for which it converges to the high LCOs in the second case. It shows the presence of basins of attraction in the system, where the lower bound is located here between Y = 0.7 and 1.1.

For the transient measurements where pressure was recorded, it is interesting to look at the lift coefficient and mostly at its frequency content. Indeed, consider Figure 4.6 where a transient signal is depicted along with the evolution of the damping ratio with amplitude and the wavelet transform of the corresponding C_L.

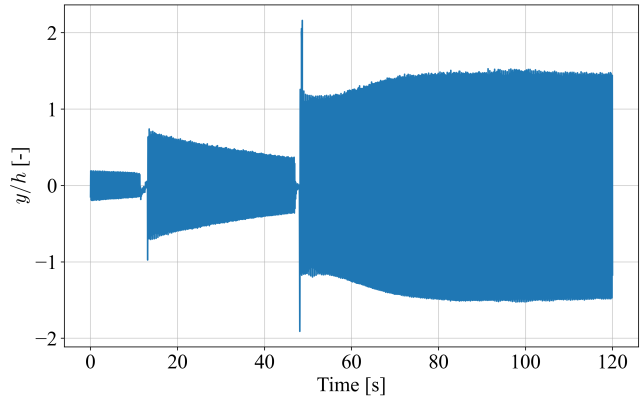

Figure 4.5: Example of the minimum initial condition, above a certain treshold wind speed, required for the system to reach LCOs for configuration (1).

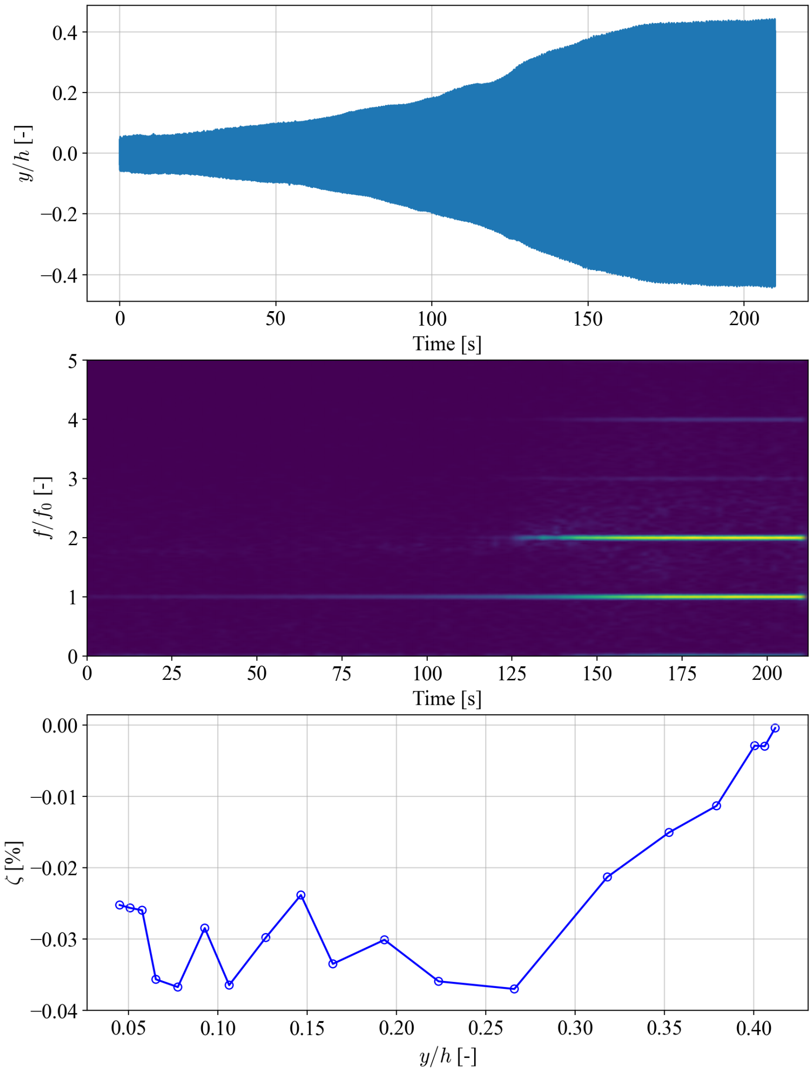

Figure 4.6: Spectral analysis of the transient experimental C_L and the corresponding damping variation.

It is found that below a certain amplitude, the vibrations occur at the natural frequency f_0 and the amplitude grows slowly. However, at some point, the second harmonic appears in the spectrum of C_L and, interestingly, it also corresponds to the moment where the amplitude starts to increase sharply, at the minimum damping point. The system seems to change regime. This is typical of a nonlinear system, where a minimal amplitude is required to activate the nonlinear effects, such as here the second harmonic.

4.3 Excitation force

The unsteady lift force due to vortex shedding C_v and the transverse force coefficient C_{F_y} from the combined numerical model will now be used to compare the excitation with the experimental pressure measurements. Indeed, the transverse force coefficient, determined experimentally as described in subsection 3.2.2, can be compared to the sum of these two contributions.

The numerical $C_v(\tau)$ is computed simply as the solution of the second equation of the combined model and is an output of the solver. The numerical C_{F_y} has to be computed from $C_{F_{y,\zeta}}$, which are linked through the relation

$$C_{F_y} = C_{F_{y,\zeta}} + \frac{2\zeta}{nU_r^{\omega}} \tag{4.1}$$

since $C_{F_{y,\zeta}}$ includes the structural damping term and which is determined using the quasi-steady seventh order polynomial (equation 2.45) with the computed $Y'(\tau)$.

The evolutions of the RMS of the transverse force coefficient determined experimentally and numerically are depicted in Figure 4.7a. As the model has been shown to generally overpredict the amplitudes of motion, especially close to the critical VIV velocity, it is expected that the amplitude of the excitation of the model is greater than the experimental one and it is indeed the case. The general trend is still the same for both numerical and experimental data. The excitation is the most different between the two for $Y < 0.5$ where VIV and galloping interact the most and are the most challenging to model. Then, as the amplitude increases, the numerical excitation decreases sharply and converges to a value of ≈ 1.1, still overestimating the experimental data. At high amplitude, the model fits better the data in terms of amplitude, as was shown, but not in terms of the excitation. As discussed before, the RMS of the excitation does not reflect the amplitude of vibration in galloping since it is not the fundamental principle of excitation of this instability, so the amplitude can still be predicted while C_{F_y} is not.

Additionally, the individual contributions of both the wake oscillator and the quasi-steady excitations are determined in Figure 4.7b. Obviously, these cannot be obtained experimentally but is it still relevant to study them. First, for C_v, a gradual increase is observed then a sharp drop, followed by the convergence to a value of 1. This shows the transition from the resonance region of VIV to the kink observed in the amplitude-velocity curves and finally to the regime where galloping takes over the system. On the other hand, for C_{F_y}, a sharp increase is observed at the location of the kink in the curve, highlighting this nonlinear phenomenon, then a progressive gradual decrease towards

≈ 0.45. Once again, the magnitude of the fluctuating force is not as important in galloping as in VIV. The experimental data lies nonetheless above the galloping contribution but below the VIV one, suggesting that the overestimation of the amplitudes probably comes from the overprediction of C_v.

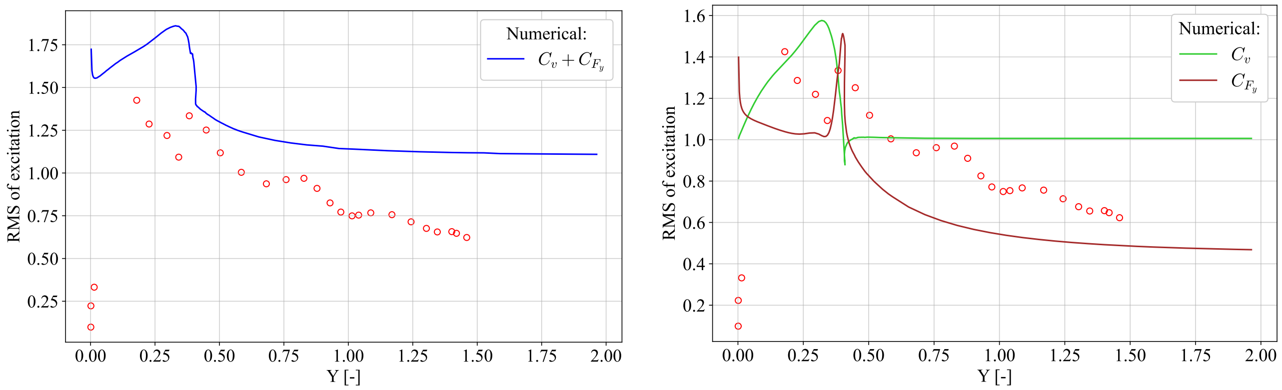

(a) Total transverse force coefficient

(b) Separated numerical contributions

Figure 4.7: Comparison between the experimental ○ and numerical transverse force coefficients in terms of the amplitude of motion, for configuration (1).

Chapter 5

Conclusions and perspectives

In this work, the interaction between two aeroelastic phenomena, namely VIV and galloping, was investigated. The high amplitudes resulting from this interaction are still not well understood nowadays, even for cylinders with simple cross sections. The square section was retained for this study. Although it has been extensively studied in terms of its general aerodynamic behavior, the coupled interaction between vortex-induced vibration and galloping remains insufficiently explored. Moreover, this geometry is still widely used in modern engineering structures.

Experimental tests were conducted in the wind tunnel facility of the university of Liège and the results were compared to a numerical model combining both instabilities. It enabled to gain insights into the mechanisms at play and assess the predictive capabilities of the model through several comparison aspects.

First, the effect of damping on the amplitude-velocity response curve was studied. Due to the very low structural damping, the amplitudes started at the critical VIV velocity and kept increasing as long as the wind speed was increased. Higher amplitudes were reached as the structural damping decreased, in accordance with the galloping theory regarding this aspect. It was also shown that the quenching of galloping by VIV implies that the quasi-steady theory fails to predict the critical airspeed at which the instability takes place.

Then, the variation of the aerodynamic coefficients in terms of wind speed was determined. The evolution of the RMS of the lift coefficient was particularly studied, and showed the transition from a VIV-like regime, where C_L^{rms} was large, to a galloping-type regime where the lift coefficient decreased with amplitude and thus airspeed. The frequency spectra of the aerodynamic force coefficients were also investigated and reavealed the presence of harmonics at odd and even multiples of the natural frequency, due to the highly nonlinear phenomena studied. These harmonics were shown to be reinforced when they coincided with the Strouhal frequency, highlighting the interaction between the fluid and the structure.

The comparison between experimental data and the numerical model was then conducted. The model overestimates the amplitudes of motion near the resonance VIV region but has good agreement with experimental data for higher amplitudes, suggesting that the modeling of the wake-oscillator system should be refined and where both phenomena interact the most.

After that, the transient build-up of oscillations was studied and it was shown that the model predicts the evolution of damping ratio in terms of amplitude quite satisfactorily in terms of trend but not in terms of value, such that the numerical system converges much faster to LCOs. The magnitude of the excitation force from both experimental and numerical data were then compared. The overestimation in the the amplitude of motion was concluded to come from the overestimation of the excitation force, especially for low amplitudes as opposed to the galloping regime, where it is less relevant.

In conclusion, the performance of the model can be improved close to the critical VIV velocity by improving the numerical modeling of the unsteady force, as the asymptotic behavior was shown to be quite well predicted. The nonlinear damping term should be revised, or another type of wake-oscillator model should be addressed.

Further work would include a wider range of damping values, enabling to study the decoupled phenomena and progressively observe a transition from partial interaction, for intermediate values of the Scruton number, to a full interaction for low values of Sc as examined here. Additionally, the pressure measurements made in this work were not synchronized in time with the transverse displacement of the cylinder. Having this synchronous data would enable to study the phase between both signals and allow correlation between both. Experimental tests could also be conducted to better identify the parameters of the numerical model, such as static tests would enable a better estimate of the polynomial coefficients of $C_{F,y}$ as it was shown that they have great influence on the solution at large reduced velocities.

Interesting aspects that have not been addressed so far would be to study the influence of the turbulence intensity and length scale on the dynamic response of the system. Furtheermore, the effect of rounded corners could be investigated. Regarding galloping only, Carassale et al. [28] already determined that turbulence tends to reduce the critical galloping velocity compared to the smooth flow case. The same was found to be the case for rounded corners since flow re-attachment is promoted and drag forces are reduced. Lastly, the surface roughness of the cylinder surface could be varied since it can significantly alter the pressure distribution around the body.

Bibliography

[1] S. Vengadesan A. Nakayama. Evaluation of les models for flow over bluff body from engineering application perspective. *Sadhana*, 2005.

[2] Collar A.R. The first fifty years of aeroelasticity. *Aerospace*, 1978.

[3] Alonso G. Barrero-Gil A., Sanz-Andrés A. Hysteresis in transverse galloping: The role of the inflection points. *Journal of FLuids and Structures*, 2009.

[4] C. Mannini A. M. Marra G. Bartoli. Viv-galloping instability of rectangular cylinders: Review and new experiments. *Journal of Wind Engineering and Industrial Aerodynamics*, 2014.

[5] C. Mannini A. M. Marra T. Massai G. Bartoli. Interference of vortex-induced vibration and transverse galloping for a rectangular cylinder. *Journal of Fluids and Structures*, 2016.

[6] C. Mannini T. Massai A. M. Marra G. Bartoli. Modelling the interaction of viv and galloping for rectangular cylinders. *14th International Conference on Wind Engineering – Porto Alegre, Brazil*, 2015.

[7] R. D. Blevins. *Flow-Induced Vibration*. Van Nostrand Reinhold, 1990.

[8] D. N. Bouclin. Hydroelastic oscillations of square cylinders. *M.ASc. Thesis, University of British Columbia*, 1977.

[9] Strouhal V. C. On a particular way of tone generation. *Wiedmann's Annalen der Physik und Chemie*, 1878.

[10] Vialta - La Passerelle de Caster. `https://www.vialta.info/`, 2025. Accessed: 2025-04-15.

[11] R. M. Corless. Mathematical modelling of the combined effects of vortex-induced vibration and galloping. *PhD thesis, The University of British Columbia*, 1986.

[12] P. W. Bearman E. D. Obasaju. An experimental study of pressure fluctuations on fixed and oscillating square-section cylinders. *Journal of Fluid Mechanics vol. 119*, 1982.

[13] Du X. et al. Aerodynamic characteristics of two closely spaced square cylinders in different arrangements. *Journal of Wind Engineering and Industrial Aerodynamics*, 2021.

[14] Y. C. Fung. An introduction to the theory of aeroelasticity. *University of California, San Diego*, 1955.

[15] Y. Tamura G. Matsui. Wake oscillator model of vortex-induced oscillation of circular cylinder. *Proceedings of the 5th International Conference on Wind Engineering*, 1979.

[16] R. M. Corless G. V. Parkinson. A model of the combined effects of vortex-induced oscillation and galloping. *Journal of Fluids and Structures*, 1987.

[17] Parkinson G.V. Mathematical models of flow-induced vibrations of bluff bodies. *Flow-Induced Structural Vibrations*, 1974.

[18] Chell Instruments. nanoDAQ-32 Miniature Intelligent Pressure Scanner. `https://chell.co.uk/absolute-pressure-scanners/nanodaq-32-miniature-intelligent-pressure-scanner/`.

[19] Kimo Instruments. Multifunction instrument ami 310. `https://m.carlssoon-tech.com/index.php?ws=showproducts&products_id=2921770&cat=Pressure-Flow`.

[20] National Instruments. What is NI LabVIEW? `www.ni.com/labview`. Accessed: 2025-05-13.

[21] Yang J. and Stern F. A simple and efficient direct forcing immersed boundary framework for fluid-structure interactions. *Journal of Computational Physics*, 2012.

[22] D. Durão J. Pereira, M. Heitor. Measurements of turbulent and periodic flows around a square cross-section cylinder. *J. Exp. FLuid.*, 1988.

[23] Y. Tamura K. Shimada. Wake oscillator model of vortex-induced oscillation of circular cylinder. *Proceedings of the International Conference on Flow-Induced Vibrations*, 1987.

[24] L. Mingyue X. Longfei Y. Lijun. Experimental investigation of flow characteristics around four square-cylinder arrays at subcritical reynolds numbers. *IJNAOE*, 2015.

[25] W. Zhang Z. Y. Zhou F. C. Cao Y. J. Ge T. C. Liu. Reynolds number on the flow around square cylinder based on latticec boltzmann method. *Proceedings of the Fifth International Conference on Fluid Mechanics*, 2007.

[26] V. Tamimi M. Dolatshahi Pirooz M. S. Seif M. Zeinoddini S. T. O. Naeeni. Effects of after-body on the fiv of a right-angle triangular cylinder in comparison to circular, square, and diamond cross-sections. *Ships and offshore structures*, 2018.

[27] L. Carassale M. Marrè-Brunenghi, A.Freda. Effects of free-stream turbulence and corner shape on the galloping instability of square cylinders. *Journal of Wind Engineering and Industrial Aerodynamics*, 2013.

[28] L. Carassale A. Freda M. Marrè-Brunenghi. Effects of free-stream turbulence and corner shape on the galloping instability of square cylinders. *Journal of Wind Engineering and Industrial Aerodynamics*, 2013.

[29] F. Biolley M.L. Facchinetti, E. de Langre. Coupling of structure and wake oscillators in vortex-induced vibrations. *Journal of Fluids and Structures*, 2004.

[30] M. Novak. Galloping and vortex induced oscillations of structures. *Proceedings 3rd International Conference on Wind Effects on Buildings and Structures, pp. 799–809*, 1971.

[31] University of Liège. The University of Liège Wind Tunnel Facility, 2009. `https://www.wind-tunnel.uliege.be`.

[32] Den Hartog J. P. Transmission line vibration due to sleet. *Transactions of the American Institue of Electrical Engineers*, 1932.

[33] de Langre E. Paidoussis M. P., Price S. J. *Fluid-structure Interactions : cross-flow induced instabilities*. Cambridge University Press, 2010.

[34] I. G. Currie R.T. Hartlen. Lift oscillator model of vortex-induced vibration. *Proceedings of the American Society of Civil Engineers, Journal of Engineering Mechanics*, 1970.

[35] A. Santosh S. C. A. Shyam. Entropic lattice boltzmann simulation of the flow pas square cylinder. *Int. J. Mod. Phys. C*, 2004.

[36] C. Scruton. Use of wind tunnels in industrial aerodynamic research. *AGARD Report 309, NPL Report 411.*, 1960.

[37] SICK. OD value OD2-P300W200I0. `https://www.sick.com/br/en/catalog/products/distance-sensors/laser-distance-sensors/od-value/od2-p300w200i0/p/p292915?tab=detail#technical-details`. Accessed: 2025-05-26.

[38] Andrianne T. Aeroelasticity and experimental aerodynamics - lecture notes. *University of Liège*, 2025.

[39] Y. Nakamura T. Mizota. Torsional flutter of rectangular prisms. *ASCE Journal of Engineering Mechanics Division*, 1975.

[40] Liège Université. Charte uliège d'utilisation des intelligences artificielles génératives dans les travaux universitaires. `https://www.student.uliege.be/cms/c_19230399/fr/faq-student-charte-uliege-d-utilisation-des-intelligences-artificielles`

[41] Karman T. V. Nachrichten von der Gesellschaft der Wissenschaften zu Göttingen, 1911.

[42] Parkison G. V. and Smith J. D. The square prism as an aeroelastic non-linear oscillator. *The Quaterly Journal of Mechanics and Applied Mathematics*, 1964.

[43] Lyn DA W. Rodi, S. Einva. A laser-doppler velocimetry study of ensemble averaged characteristics of the turbulent near wake of a square cylinder. *J. Fluid Mech.*, 1991.

[44] R. Franke W. Rodi. Calculation of vortex shedding past a square cylinder with various turbulence models. *Proc. 8th Symp. Turbulent Shear Flows, 1991, Tech. Univ. Munich, Springer Berlin*, 1991.